

JGR Earth Surface

RESEARCH ARTICLE

10.1029/2024JF008067

Special Collection:

Modeling of Geological Hazards
in Complex Environments

Key Points:

- A new framework was developed to assess glacial lake outburst floods by integrating remote sensing and hydrological models
- The study found that Jiongpu Co expanded significantly, with potential avalanche and landslide runouts posing serious flood threats
- We simulated the GLOF process with glacier avalanches and landslide runouts into the lake and then evaluated downstream flooding parameters

Correspondence to:

Z. Lu,
zhonglu@smu.edu

Citation:

Yang, L., Lu, Z., Zhao, C., Hu, X., & Wang, B. (2025). Studying mass movement sources and potential glacial lake outburst flood at Jiongpu Co, southeastern Tibet, using multiple remote sensing methods and HEC-RAS model.

Journal of Geophysical Research: Earth Surface, 130, e2024JF008067. <https://doi.org/10.1029/2024JF008067>

Received 3 OCT 2024
Accepted 7 JUL 2025

Author Contributions:

Conceptualization: Zhong Lu
Formal analysis: Liye Yang,
 Chaoying Zhao, Xie Hu, Baohang Wang
Funding acquisition: Chaoying Zhao
Methodology: Liye Yang
Resources: Zhong Lu
Software: Liye Yang
Writing – original draft: Liye Yang
Writing – review & editing: Liye Yang,
 Zhong Lu, Chaoying Zhao, Xie Hu,
 Baohang Wang

© 2025. The Author(s).

This is an open access article under the terms of the [Creative Commons](#)

[Attribution License](#), which permits use, distribution and reproduction in any medium, provided the original work is properly cited.

Studying Mass Movement Sources and Potential Glacial Lake Outburst Flood at Jiongpu Co, Southeastern Tibet, Using Multiple Remote Sensing Methods and HEC-RAS Model



Liye Yang^{1,2}, Zhong Lu^{3,4} , Chaoying Zhao², Xie Hu⁵ , and Baohang Wang⁶

¹College of Civil Engineering, Xiangtan University, Xiangtan, China, ²School of Geological Engineering and Geomatics, Chang'an University, Xi'an, China, ³Roy M. Huffington Department of Earth Sciences, Southern Methodist University, Dallas, TX, USA, ⁴School of Environment and Spatial Informatics, China University of Mining and Technology, Xuzhou, China, ⁵College of Urban and Environmental Sciences, Peking University, Beijing, China, ⁶School of Geography and Oceanography, Minjiang University, Fuzhou, China

Abstract Glacial lake outburst floods (GLOFs) caused by mass movement into lakes are common disaster chains in High Mountain Asia (HMA). However, the volumes of potential avalanche sources and the associated overtopping flood processes remain inadequately understood, hindering GLOF hazard assessments. We developed a comprehensive framework to quantify mass movement volumes and simulate GLOF process chains by integrating remote sensing data with hydrological models. We applied our methodology to Jiongpu Co, the largest glacial lake in southeastern Tibet. First, analysis of optical images revealed lake expansion from 2000 to 2024. Second, we assessed the volume of potential glacier avalanche using three-dimensional glacier velocities from multi-track Synthetic Aperture Radar (SAR) images. The estimated volume is $1.8 \pm 0.06 \times 10^8 \text{ m}^3$. Third, deformation on the surrounding slopes was investigated based on the time-series InSAR method, revealing a potential landslide volume of $3.5 \pm 0.2 \times 10^8 \text{ m}^3$. Next, we retrieved overtopping volumes from the potential glacier avalanche and landslide, which are $1.94 \pm 0.1 \times 10^7 \text{ m}^3$ and $9.89 \pm 0.6 \times 10^7 \text{ m}^3$, respectively. Finally, we evaluated the GLOF process chain under these two scenarios using the HEC-RAS model. Our integrated approach enhances GLOF monitoring and modeling, offering applicability to other glacial lakes for risk assessment and mitigation.

Plain Language Summary Glacial lake outburst floods (GLOFs) are a significant risk in High Mountain Asia, often triggered by glacier avalanches or landslides into lakes. However, investigations on the volume of potential landslide sources and the resulting flood processes are lacking, making it difficult to assess GLOF hazards. In our study, we developed a framework that combines remote sensing and hydrological models to estimate the volume of mass movements and simulate GLOF processes. We focused on Jiongpu Co, the largest glacial lake in southeastern Tibet. The lake area nearly doubled between 2000 and 2024. We estimated the volume of potential glacier avalanches at $1.8 \pm 0.06 \times 10^8 \text{ m}^3$ and identified a possible landslide volume of $3.5 \pm 0.2 \times 10^8 \text{ m}^3$. We calculated potential flood volumes from these events, which were 19.4 ± 1.0 million m^3 for the glacier avalanche and 98.9 ± 6.0 million m^3 for the landslide. Using the HEC-RAS model, we evaluated the flooding discharge and depth under two scenarios. These findings highlight the urgent need for effective risk management strategies for GLOFs, as our integrated approach can be applied to other glacial lakes to enhance hazard assessment and mitigation efforts.

1. Introduction

Glacier mass loss is accelerating, and glacial lakes are expanding rapidly due to climate warming across the globe (Zheng et al., 2021). Of particular concern is the growing threat of cascading disasters linked to glacial lake outburst floods (GLOFs) (S. K. Allen et al., 2019; Cook et al., 2018; Y. Li et al., 2024). GLOF hazards are represented by the abrupt and swift discharge of large water volumes from glacial lakes, affecting livelihoods and infrastructure for tens or hundreds of kilometers downstream (Y. Li et al., 2024; Sattar et al., 2023). Research has revealed that impulse displacement waves from glacier avalanches or landslides impacting stored lake water account for 41.24% of GLOFs (X. Lu et al., 2022). In contrast, only 28.10% of GLOFs are attributed to the melting of buried ice, significant rainfall, or the gradual failure of lake dams (X. Lu et al., 2022). Hence, most catastrophic

dam failures result from displacement waves created by the significant impact of ice or falling rocks (Y. Li et al., 2024; Nie et al., 2018). The size of wave-overtopping-induced glacial lake outbursts can be up to eight times that of glacial lake outbursts without wave-overtopping (H. Chen et al., 2017). In addition, dam overtopping, dam failure, and downstream flood hazards occur due to displacement of lake or reservoir water by landslide movements or glacial advances, including those associated with GLOFs (Delaney & Evans, 2015; Y. Li et al., 2024; Liu et al., 2019). Therefore, GLOFs caused by mass movement into lakes or reservoirs hold greater engineering significance than other non-wave-related outbursts.

Glacier avalanches directly impact the proglacial lakes by generating huge displacement waves (Sattar et al., 2023; Shugar et al., 2021). An increase in multi-temporal imagery and topographic data from remote sensing platforms has facilitated the GLOF hazard assessment (e.g., S. K. Allen et al., 2019; Sattar et al., 2023). Glacier avalanches can be detected through optical imagery and slope classification derived from Digital Elevation Models (DEMs). However, the volume of glacier avalanche is difficult to estimate due to strong assumptions and unrealistic parameters in High Mountain Asia (HMA) areas (Bahr et al., 1997; Frey et al., 2014). The distribution of ice thickness and volume has a great influence on GLOF chain modeling. Consequently, obtaining the volume of glacier avalanche helps to model the overtopping volume and floods downstream in the GLOF process.

Slope instability caused by glacier retreating and permafrost melting can lead to large-scale glacier detachment in low-angle valleys, such as the collapse of the Aru Twin Glacier in 2016 (Kääb et al., 2018). After glacier retreat, exposed valley slopes can lose stability due to debuttressing effects (Antoniazza & Lane, 2021; Dai et al., 2020; Savi et al., 2021). Additionally, permafrost degradation during the thaw season can contribute to slope instability (Antoniazza & Lane, 2021; Savi et al., 2021). In HMA regions, the scale and occurrence of slope instability are increasing, and this trend is projected to persist in the coming years (S. K. Allen et al., 2011; Savi et al., 2021). Therefore, regular monitoring of surrounding slopes above glacial lakes using remotely sensed data is highly recommended. The interferometric synthetic aperture radar (InSAR) technique is an essential tool for obtaining important deformation observations of slopes in paraglacial environments (e.g., Kim et al., 2022; Z. Lu & Kim, 2021; L. Yang et al., 2022).

Southeastern Tibet experiences frequent GLOFs; for example, Ranzerio outburst occurred in 2013 was caused by a glacier avalanche into the lake (Peng et al., 2023; Sun et al., 2014; X. Wang & Liu, 2016). In 2020, Jinweng Co (“Co” means “lake” in the Tibetan language) experienced an outburst flooding that induced huge financial loss and damaged structures downstream (Peng et al., 2023; L. Yang et al., 2022). Jiongpu Co, the largest glacial lake in southeastern Tibet, has the most significant increase in its volume (Zhang et al., 2023). The parent glacier of Jiongpu Co lost a huge mass of over 0.26 Gt from 2000 to 2020 (Zhang et al., 2023). Therefore, monitoring and modeling glacial lake hazards on Jiongpu Co hold substantial theoretical research value and practical engineering significance.

In this study, we aim to monitor the potential mass movement using satellite-based remote sensing methods and to model the GLOF process with hydrometrical models at Jiongpu Co, providing insights into a comprehensive understanding of the GLOF hazard chain. Our specific objectives include (a) mapping long-term area expansion of the glacial lake with Landsat-based optical images; (b) inverting the parent glacier thickness from three-dimensional (3-D) flow velocities via offset tracking methods with multi-track Sentinel-1 images; (c) estimating the volume of potential glacier avalanche based on thickness result and topographic slope threshold; (d) monitoring deformation at the surrounding slopes above the lake using time-series InSAR method and estimating potential landslide volume; (e) modeling GLOF processes, evaluating flood discharges and depths based on the estimated overtopping volumes using HEC-RAS model. Overall, this study employs multiple remote sensing methods to investigate the 3-D glacier dynamics, slope deformation, volumes of potential initial sources, and overtopping volumes. Furthermore, these significant remote sensing measurements were used to model the GLOF chain and evaluate GLOF hazards. Our study demonstrates the integration of remote sensing methods and hydrometrical models for GLOF hazards in HMA areas.

2. Study Area and Its Significance

Jiongpu Co and its parent glacier are situated in Bomi County in the southeastern Tibetan Plateau. In this region, glacial meltwater is critical for sustaining major river systems in South and Southeast Asia (Immerzeel et al., 2010). The study area experiences the longest annual rainy season driven by the South Asian monsoon,

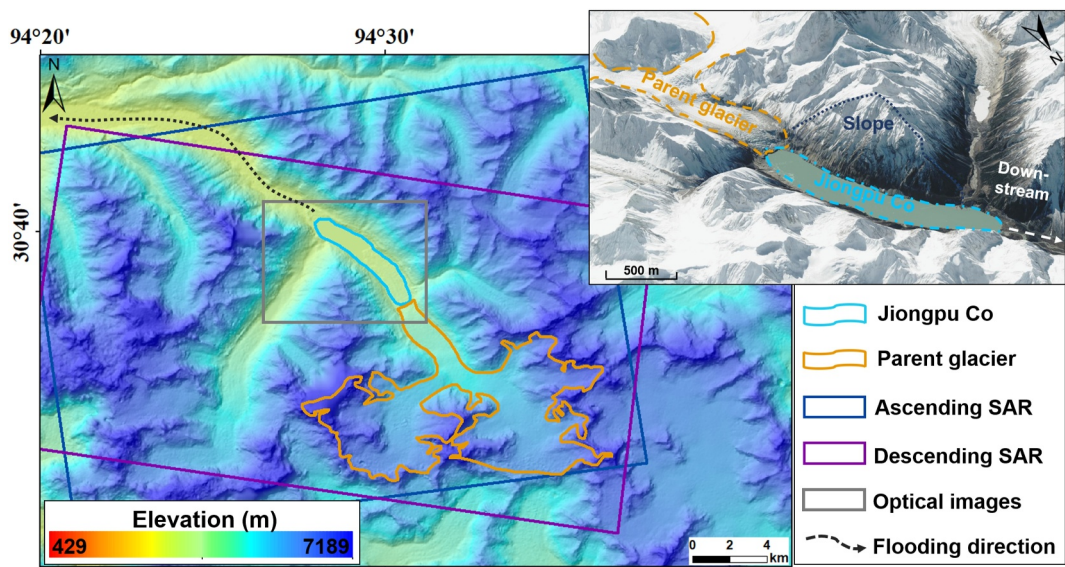


Figure 1. The overview of the study area features Jiongpu Co, its parent glacier, and the footprints of the multi-source remote sensing data sets. An inset map derived from Google Earth imagery highlights key features: parent glacier, Jiongpu Co, surrounding slopes, and downstream river reaches.

which enters the region through the Grand Bend of the Yarlung Tsangpo River (W. Yang et al., 2013). The annual mean temperature in the area is 9.0°C, with January (the coldest month) averaging 0.3°C and July (the warmest month) recording 16.7°C (W. Yang et al., 2013). The rainy season typically lasts for almost 7 months, from March to October, during which over 80% of annual precipitation occurs (W. Yang et al., 2013).

Jiongpu Co underwent the most significant volumetric expansion from 2000 to 2020. The parent glacier of Jiongpu Co lost 0.26 ± 0.12 Gt of mass during 2000–2020. This level of glacier mass loss is significant, exceeding 0.2 Gt. It is one of the highest estimated mass losses among glaciers in Tibet (Zhang et al., 2023). Hence, the research on potential lake outburst floods in Jiongpu Co is significant for assessing hazard risk and developing prevention and mitigation. However, existing studies remain limited in simultaneously investigating glacier dynamics, slope movements, and GLOF processes. Therefore, we integrated multi-source remote sensing data sets for a thorough investigation of Jiongpu Co in southeastern Tibet. These data sets include optical images and ascending and descending SAR images, as illustrated in Figure 1.

3. Data sets and Methods

About 74 ascending (blue rectangle in Figure 1) and 49 descending (magenta rectangle in Figure 1) C-band Sentinel-1 SAR images were utilized to illustrate the 3-D glacier dynamics and slope movements in our study area. Landsat-based optical images of 25 scenes were acquired to document the spatiotemporal expansion of Jiongpu Co, as indicated by the gray rectangle in Figure 1. We collected daily precipitation data sets from the Global Precipitation Measurement (GPM) mission (Skofronick-Jackson et al., 2017). Historical daily weather temperatures were obtained from a weather platform (<https://lishi.tianqi.com/bomi/index.html>), given the absence of in situ meteorological stations. Previous studies have validated that ambient temperatures recorded at this external site are representative of regional thermal conditions (W. Wang et al., 2018). Detailed information on the remote sensing data sets employed is presented in Table 1.

First, the lake area and volume were calculated using Landsat-based optical images to monitor the lake's evolution. Second, we obtained the 3-D glacier velocities using Pixel Offset tracking and Multidimensional Small Baseline Subsets (SBAS) (PO-MSBAS) method with ascending and descending Sentinel-1 images. We estimated slope deformation based on the time series InSAR method with ascending Sentinel-1 images. We then retrieved the volume of potential glacier avalanche and slope failures using these remote sensing observations. Next, we simulated the potential GLOF processes based on the HEC-RAS model, considering the scenarios of a glacier

Table 1
Characteristics of Remote Sensing Data in This Study

Data sets	Time	Pixel spacing (m)	Number of images	Objectives
Ascending Sentinel-1	2019–2022	2 × 14 (range × azimuth)	74	Deformation monitoring of glacier and glacial lake
Descending Sentinel-1	2019–2022	2 × 14 (range × azimuth)	49	
Landsat-7 ETM+	2000–2014	30	15	Lake area changes
Landsat-8 OLI	2015–2024	30	10	

avalanche and a landslide flowing into the lake, respectively. Figure 2 presents a flowchart illustrating the multiple remote sensing methods and the hydrodynamic model.

3.1. Mapping Area and Volume of Jiongpu Co With Optical Images

To track glacial lake dynamics, we acquired historical Landsat images and calculated lake area using the Normalized Difference Water Index (NDWI). NDWI maps were derived using two band combinations: NIR-green and SWIR-green (e.g., F. Chen et al., 2021; Gardelle et al., 2011; Nie et al., 2013). A total of 25 Landsat7/8 scenes spanning 2000–2024 were collected. For Landsat 8, SWIR bands were prioritized due to their demonstrated superiority in water classification compared to NIR bands (Du et al., 2014; W. Li et al., 2013). The NDWI values were computed as follows:

$$\begin{cases} \text{Landsat7} = \frac{\text{Band2}_{\text{Green}} - \text{Band4}_{\text{NIR}}}{\text{Band2}_{\text{Green}} + \text{Band4}_{\text{NIR}}} \\ \text{Landsat8} = \frac{\text{Band3}_{\text{Green}} - \text{Band6}_{\text{SWIR}}}{\text{Band3}_{\text{Green}} + \text{Band6}_{\text{SWIR}}} \end{cases} \quad (1)$$

The NDWI values were then used to generate binary classifications of glacial lakes via thresholding (Gardelle et al., 2011; Nie et al., 2013). Here, some of the winter optical images were not accurately segmented due to snow coverage, so we manually obtained the boundaries of glacial lakes. Moreover, these vectorized lake boundaries were examined by combing the original optical images and existing data sets (X. Wang et al., 2020; Zhang et al., 2015) to ensure a consistent output.

Thereafter, we calculated the mean depth and volume of Jiongpu Co using the empirical relationship (Fujita et al., 2013):

$$\begin{cases} d_m = 55 \times a^{0.25} \\ V_{\text{lake}} = a \times d_m \times 10^{-3} \end{cases} \quad (2)$$

where d_m represents the mean depth of the lake (in m), a represents the lake area (in km^2), and V_{lake} represents the lake volume (in km^3).

3.2. Monitoring Potential Glacier Avalanches With SAR Data sets

First, we derived 3-D glacier flow velocities from multi-track Sentinel-1 SAR images using the PO-MSBAS method. We then retrieved glacier thickness distributions from 3-D glacier velocities. Finally, we estimated the volume of potential glacier avalanche by integrating the derived thickness with the criteria of topographic slope.

3.2.1. Monitoring 3-D Glacier Velocities With PO-MSBAS Method

We processed a total of 74 ascending and 49 descending Sentinel-1 images from January 2019 to December 2021 to derive 3-D glacier velocities using the PO-MSBAS method. The thresholds for the temporal and spatial baselines were set to 60 days and 200 m, respectively, for creating offset pairs. The maximum perpendicular baseline reached 169 and 142 m for the ascending and descending SAR data sets, respectively. The maximum temporal baseline for both ascending and descending SAR images was 60 m. In response, 250 ascending image

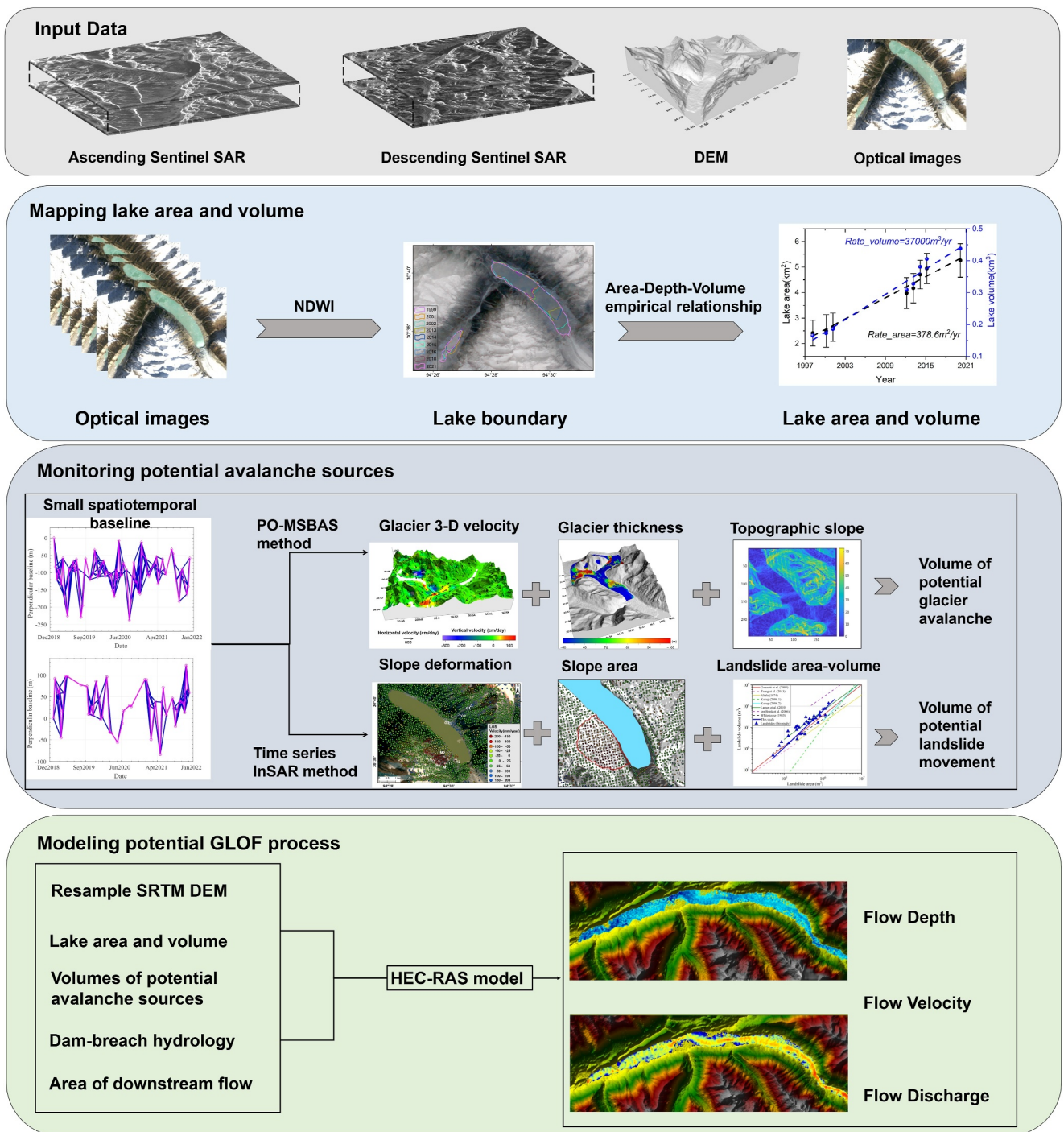


Figure 2. Flowchart of remote sensing data, monitoring of avalanche sources, and modeling of GLOF processes.

pairs (one subset) and 123 descending image pairs (three subsets) were formed (Figure 3). To construct 3-D glacier displacement time series, we connected the long-term displacement time series by fitting the time series in each of the three subsets and filling the deformation gaps in the missing data period via linear interpolation (Chang & Hanssen, 2015).

Offset tracking was performed using GAMMA software, which employs the normalized correlation coefficient to track offsets between SAR images (Guo et al., 2020; L. Yang et al., 2020, 2022). We applied a correlation coefficient threshold of 0.1 to filter unreliable offsets. The 1-arc-second Shuttle Radar Topography Mission (SRTM)

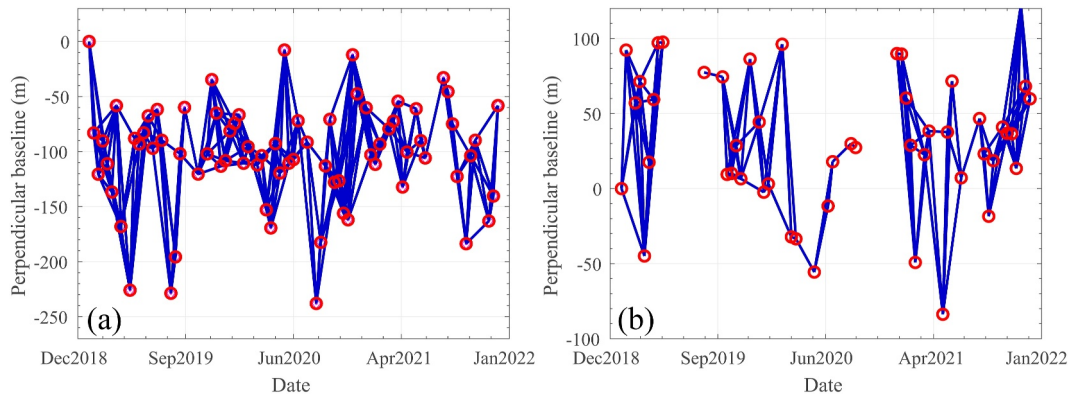


Figure 3. Configurations of spatiotemporal baselines of PO-MSBAS. (a) Ascending Sentinel-1 data sets. (b) Descending Sentinel-1 data sets. The blue lines represent the offset tracking pairs. The red circles represent the SAR images.

DEM was utilized to facilitate image co-registration. The offset-tracking procedure employed a 128×128 -pixel matching window (range \times azimuth) and a 4×1 pixel search step (range \times azimuth). Offsets for each pixel were calculated in four directions: ascending line-of-sight (LOS), ascending azimuth, descending LOS, and descending azimuth. These measurements were then used to drive 3-D glacier velocities and displacement time series.

The PO-MSBAS method was employed to derive 3-D glacier displacement time series. Pixel-offset observations served as inputs for the MSBAS model. Based on four displacement measurements from ascending and descending tracks, the 3-D displacement field was inverted using the equations presented in Equation 3 (Guo et al., 2020; J. Li et al., 2018; L. Yang et al., 2020):

$$\begin{cases} d_{los}^A = d_N \sin \theta^A \cos\left(\alpha^A - \frac{3\pi}{2}\right) + d_E \sin \theta^A \sin\left(\alpha^A - \frac{3\pi}{2}\right) - d_U \cos \theta^A \\ d_{los}^D = d_N \sin \theta^D \cos\left(\alpha^D - \frac{3\pi}{2}\right) + d_E \sin \theta^D \sin\left(\alpha^D - \frac{3\pi}{2}\right) - d_U \cos \theta^D \\ d_{az}^A = d_N \sin\left(\alpha^A - \frac{3\pi}{2}\right) - d_E \cos\left(\alpha^A - \frac{3\pi}{2}\right) \\ d_{az}^D = d_N \sin\left(\alpha^D - \frac{3\pi}{2}\right) - d_E \cos\left(\alpha^D - \frac{3\pi}{2}\right) \end{cases} \quad (3)$$

where d_{los}^A , d_{los}^D , d_{az}^A , and d_{az}^D represent the LOS displacement of ascending SAR images, LOS displacement of descending SAR images, azimuth displacement of ascending SAR images, azimuth displacement of descending SAR images, respectively. A represents the ascending track, whereas D represents the descending track; θ represents the incidence angle; α represents the flight azimuth angle; E , N , and U refer to the east, north, and vertical directions. The matrix can be represented as follows:

$$\underbrace{\begin{bmatrix} \sin \theta^A \sin\left(\alpha^A - \frac{3\pi}{2}\right) & \sin \theta^A \cos\left(\alpha^A - \frac{3\pi}{2}\right) & -\cos \theta^A \\ \sin \theta^D \sin\left(\alpha^D - \frac{3\pi}{2}\right) & \sin \theta^D \cos\left(\alpha^D - \frac{3\pi}{2}\right) & -\cos \theta^D \\ -\cos\left(\alpha^A - \frac{3\pi}{2}\right) & \sin\left(\alpha^A - \frac{3\pi}{2}\right) & 0 \\ -\cos\left(\alpha^D - \frac{3\pi}{2}\right) & \sin\left(\alpha^D - \frac{3\pi}{2}\right) & 0 \end{bmatrix}}_B = \underbrace{\begin{bmatrix} d_e \\ d_n \\ d_u \end{bmatrix}}_X = \underbrace{\begin{bmatrix} d_{los}^A \\ d_{los}^D \\ d_{az}^A \\ d_{az}^D \end{bmatrix}}_L \quad (4)$$

where, the design matrix B composes imaging geometry parameters. Matrix X represents the east, north, and vertical glacier displacements. Matrix L composes the displacements in four directions. Equation 4 can be solved by singular value decomposition (SVD) to obtain 3-D glacier velocity and displacement time series.

3.2.2. Inferring Glacier Thickness Based on 3-D Flow Velocities

We used the thickness inversion method based on the 3-D glacier velocities. Previous studies (Farinotti et al., 2017, 2021; Glen, 1955; Morlighem et al., 2011) suggested the glacier as an incompressible medium. The glacier thickness can be expressed by the divergence of ice flux and the local mass balance rate:

$$\frac{\partial H}{\partial t} = -\nabla \cdot (\bar{u}H) + M \quad (5)$$

where, $\frac{\partial H}{\partial t}$ represents the change in glacier thickness. \bar{u} represents depth-averaged glacier velocity. H represents the thickness of glacier, and M represents the local mass balance rate. In our study area, we used the geodetic glacier mass balance rate in previous studies in the same period, showing that the glacier mass change is -0.7 ± 0.13 m.w.e, -0.4 ± 0.10 m.w.e, -0.1 ± 0.05 m.w.e in 2019, 2020, 2021 years, respectively (Hugonet et al., 2021; Luo et al., 2023).

Note that the depth-averaged velocity \bar{u} of glaciers is not identical to surface velocity u_{surf} . It can be calculated with the surface velocity u_{surf} and the rheological parameter $f : \bar{u} = fu_{\text{surf}}$ (Delbridge et al., 2016; Hu et al., 2018). For glaciers with ice frozen to the bed, the depth-averaged velocity can be up to 15% lower than the surface velocity (Hu et al., 2018, 2019; Millan et al., 2022).

In our study, we based the rheology choice on glacier velocity and terrain slope. When the slope of the glacier is nearly flat, it often leads to an overestimation of glacier thickness. Additionally, surging glaciers further contribute to this overestimation (Delbridge et al., 2016; Millan et al., 2022; Morlighem et al., 2011). Thus, we used the ratio between the terrain slope and glacier's surface velocity to parametrize the rheological parameter. Based on earlier research (Millan et al., 2022), when the ratio exceeds 0.001, the rheological parameter f is set to 0.1, which indicates that glacier deformation plays a major role in glacier movement. The rheological parameter f is modulated to 0.9 where the ratio is less than 0.001. Therefore, we updated the rheological parameter of the parent glacier to derive the optimum glacier thickness.

Then, Equation 5 can be simplified under the assumption that the glacier elevation of its basal surface remains constant over a short duration:

$$\frac{\partial z}{\partial t} = -\nabla \cdot (fu_{\text{surf}}H) + M \quad (6)$$

where $\frac{\partial z}{\partial t}$ shows the elevation change measured by vertical velocity, f represents the rheological parameter, u_{surf} represents the surface horizontal velocity, H represents the glacier thickness, and M represents the local mass balance rate. Equation 6 can be estimated on a finite difference grid and written in the following form:

$$\tilde{U}\tilde{H} = \tilde{M} \quad (7)$$

where \tilde{U} is a matrix containing glacier horizontal velocity u_{surf} , which is calculated by $\sqrt{V_E + V_N}$, $\tilde{H} = f \cdot H$ is a vector of the unknown thickness scaled by rheological parameter, \tilde{M} is a vector containing the mass balance rate and vertical velocity V_U . Here we built up the relationship between the glacier's 3-D velocity and thickness. Then, we used a least-squares solution to obtain stable thickness results.

3.2.3. Mapping Volume of Potential Glacier Avalanche

Following the derivation of glacier thickness, we assessed the potential avalanche volume using topographic slope criteria. Based on a global inventory of ice and rock avalanche events, the critical slope threshold for triggering glacier avalanches is 14° (S. K. Allen et al., 2019). Slopes exceeding 14° were identified as high-risk areas where avalanches pose a threat to glacial lakes (S. K. Allen et al., 2019; Sattar et al., 2023). Here, the

potential glacier avalanche volume was estimated by integrating the derived thickness with slope-threshold-defined areas.

3.3. Monitoring Landslide Movement With Time Series InSAR

Ascending Sentinel-1 SAR images from 2019 to 2021 were utilized to derive slope deformation and identify destabilization zones above Jiongpu Co using the MTI method, including Persistent Scatterer InSAR (PS-InSAR) and SBAS-InSAR algorithm (Berardino et al., 2002; Ferretti et al., 2001; Hooper, 2008; Qin et al., 2024). We used the MTI Method based on the Stanford Method for Persistent Scatterers (StaMPS) (Azadnejad et al., 2020; Hooper, 2008; Hooper & Zebker, 2007). The cropped interferograms were processed at full spatial resolution. In the PS-InSAR method, PS candidates were initially analyzed based on amplitude (Ferretti et al., 2001; Qu et al., 2023). Slowly varying filtered phase (SFP) pixels were identified among the candidate pixels in a similar way to PS pixels. PS pixels were selected based on single-reference interferograms without spectral filtering, whereas SFP pixels were selected based on multi-reference small-baseline interferograms with spectral filtering (Hooper, 2008; Hooper et al., 2004; Qu et al., 2023; L. Yang et al., 2023). The interferograms selected for the SBAS method have time intervals, vertical baselines, and Doppler shifts below a certain threshold to maximize interferometric coherence (Berardino et al., 2002; Hooper, 2008). Range and azimuth filters were applied to the images to minimize the effects of non-overlapping Doppler spectra and geometric uncorrelation (Qu et al., 2023). In this MTI method, the interferograms are also deramped to eliminate residual orbital errors and long-wavelength atmospheric errors (Hooper, 2008).

By combining PS-InSAR and SBAS methods, MTI increases the spatial density of available signals (Hooper, 2008; Qu et al., 2023). The combined phase of the SBAS interferometric measurements consisting of PS and SFP pixels was subsequently subjected to 3D phase unwrapping (Hooper, 2008; Hooper & Zebker, 2007). Atmospheric artifacts and baseline errors were then estimated and removed by temporal high-pass filtering and spatial low-pass filtering (Qu et al., 2023). The corrected unwrapped phases from selected small baseline interferograms are then inverted using the least squares method to determine the time-series phase of all pixels.

After mapping active landslides based on deformation rates, the landslide volume was calculated based on the area-volume relationship. Numerous studies have employed power-law functions to establish the relationship between landslide volume and area (Kang et al., 2023; Korup, 2006; Tseng et al., 2013). In this study, we utilized the area-volume relationship of landslides proposed by Korup (2006), which was derived from 333 samples in high-mountainous areas. The relationship between landslide volume V_l (km^3) and area A_l (km^2) can be expressed as:

$$V_l = \alpha A_l^\beta \quad (8)$$

where $0.01 \leq \alpha < 0.05$ and $1.30 \leq \beta < 2.56$. These values are obtained from landslide data collected across different mountain ranges in high-altitude regions (Korup, 2006).

3.4. Modeling GLOF Processes With HEC-RAS Model

In our study, based on the identified potential glacier avalanches and landslides, we conducted potential GLOF hazard assessments involving initial source movements into the lake, wave run-up, overtopping volume, and downstream flooding (Figure 4). The GLOF process chain was simulated using the HEC-RAS model, which has been widely applied in flood hazard assessments (Sattar et al., 2023; W. Yang et al., 2023). Using the remote sensing-derived potential initial source movements into the lake, we examined two GLOF scenarios. These scenarios have different magnitudes based on the estimated release volumes in Sections 3.2–3.3. We used a resampled SRTM DEM of 12.5 m to represent the terrain condition in this GLOF model. The initial source volumes, including potential glacier avalanche and the landslide, are critical parameters for modeling the GLOF process chain.

Figure 4 illustrates the key dam parameters and the potential GLOF process chain, highlighting wave propagation and dam overtopping. To simulate the GLOF process chain, we assessed overtopping volumes based on initial source volumes and dam parameters (X. Lu et al., 2022). A method for estimating glacial lake impulse wave overtopping was proposed by X. Lu et al. (2022) and validated through experimental and numerical investigations. The overtopping volume V_{ot} is proportional to the run-up volume V_{rp} :

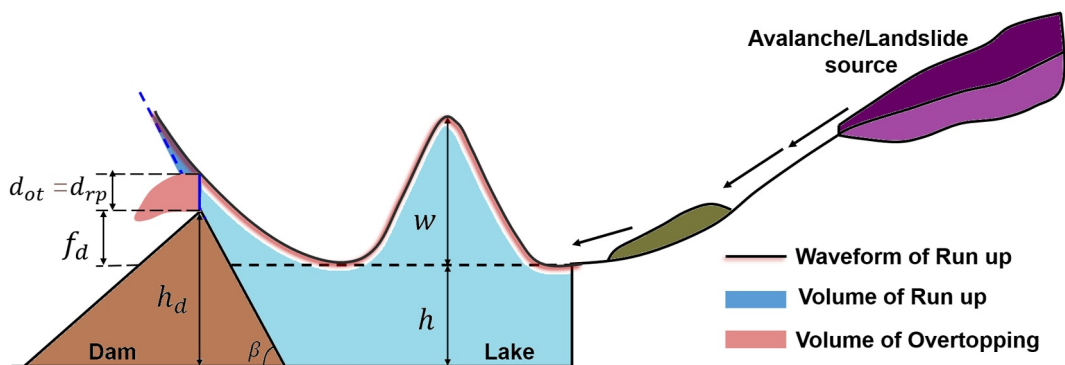


Figure 4. Schematic diagram showing the dam parameters and GLOF process. h refers to the mean depth of the lake; w refers to the wave amplitude; h_d refers to the dam height; d_{ot} and d_{rp} refer to the overtopping and run-up depths at the dam's crest, respectively; β refers to the angle of dam upstream; and f_d refers to the difference between h_d and h .

$$V_{ot} = k V_{rp} \quad (9)$$

where k is the ratio of the overtopping volume to the run-up volume. The run-up volume arises from the initial potential mass movement into the lake. Experimental investigations were conducted to derive the equation of volume ratio k (X. Lu et al., 2022):

$$k = e^{0.319} (\tan \beta)^{2.210} (w/h)^{-1.093} [(f_d + w)/w]^{1.606} \quad (10)$$

where β represents angle of dam toe upstream; w represents the wave amplitude; h represents the mean depth of the lake; f_d refers to difference between h_d and h .

Here, we calculated the run-up volume based on initial source volumes. In this study, we set $\beta = 15^\circ$ (X. Lu et al., 2022). The lake area, depth, and volume of Jiongpu Co were estimated using Landsat-8 optical images and empirical relationship derived from Fujita et al. (2013). Based on Equation 2, the lake area a , mean depth h and volume were 5.31 km^2 , 83 m , and $443 \times 10^6 \text{ m}^3$, respectively. The wave amplitude w was calculated based on the initial source volume V_{pm} and the lake area $a : w = V_{pm}/a$. h_d is the dam height derived from terrain data. Then, f_d is calculated by subtracting the lake depth from the dam height. Hence, we obtained the overtopping volume for varying glacier avalanches and the landslide source. Given that HEC-RAS simulates dam breach processes using empirical methods developed for earthen embankments, the moraine-dammed Jiongpu Co was approximated as a simplified embankment dam to facilitate breach modeling within the framework.

The Manning roughness coefficient was determined based on land cover and vegetation, with a recommended range of 0.025–0.033, yielding an average value of 0.03 (Sattar et al., 2023). Therefore, we assigned a Manning parameter of 0.03 for the downstream channel, where vegetation is absent (Sattar et al., 2023; L. Yang et al., 2023). We employed the complete momentum equation in our analysis, using a simulation time step of 1 s and a total duration of 24 hr. We performed the 2D unsteady flow calculations based on the HEC-RAS model. The upstream boundary conditions were supplied by estimated dam-breach hydrographs. The downstream boundary conditions were set to a normal water depth of 0.01 m/m (Sattar et al., 2023; L. Yang et al., 2023). Finally, we assessed flow depth and discharge at three cross-sections along the flow channel located 1 km (Jinlingcun, village 1), 9 km (Jitangcun, village 2), and 11 km (Jiecun, village 3) downstream of the lake.

3.5. Uncertainty Analysis

The uncertainty on lake area estimation for a single glacial lake was assessed using a margin of ± 0.5 pixels inside/outside the delineated boundary (Fujita et al., 2009; Zhang et al., 2023), represented as:

$$\delta A_i = P_i \times \frac{G_i}{2} \quad (11)$$

where δA_i represents the uncertainty area of each glacial lake. P_i denotes the perimeter of glacial lakes. G_i refers to the spatial resolution of Landsat-based optical images, which is 30 m used in this study.

Here, we used PO-MSBAS and InSAR methods to characterize the movement of glaciers and slopes. Uncertainties in 3-D glacier velocities (δ_{V_E} , δ_{V_N} , δ_{V_U}) and slope deformation were estimated by calculating the standard deviation (STD) in stable areas due to the absence of in situ ground motion measurements. This method has been validated in previous studies where the study area was located in environmentally hostile regions (Ali et al., 2020; Yan et al., 2015). When the STD values in a stable region are much lower than the average deformation rate, this indicates the reliability of the result.

Based on Equation 7, thickness results were derived from 3-D glacier velocities and mass balance rate. The uncertainties of glacier thickness were estimated using error propagation techniques, as shown in Equation 12:

$$\delta_H = \sqrt{\left(-\frac{V_E \cdot \tilde{M}}{\left(\sqrt{V_E^2 + V_N^2}\right)^3} \right)^2 \delta_{V_E}^2 + \left(-\frac{V_N \cdot \tilde{M}}{\left(\sqrt{V_E^2 + V_N^2}\right)^3} \right)^2 \delta_{V_N}^2 + \left(\frac{1}{\sqrt{V_E^2 + V_N^2}} \right)^2 \delta_{\tilde{M}}^2} \quad (12)$$

where δ_H , δ_{V_E} , δ_{V_N} , $\delta_{\tilde{M}}$ represent the STD values of the thickness term, east-west velocity component, north-south velocity component, and mass balance term, respectively. V_E and V_N represent glacier velocity in east-west and north-south directions, respectively. \tilde{M} represents glacier mass balance rate and glacier vertical velocity V_U . Then, the uncertainty in the volume of the glacier avalanche can be calculated from $\delta_{V_g} = a_g \cdot \delta_H$, where a_g represents the area of potential glacier avalanche calculated by slope criteria. For a potential landslide into the lake, the uncertainty of the landslide volume was calculated by $\delta_{V_l} = \alpha \delta_{A_l}^\beta$ based on Equation 8, where $\delta_{A_l} = P_{A_l} \cdot G_{A_l}/2$ can be estimated by perimeter P_{A_l} of the deformed area and the spatial resolution G_{A_l} . Then, the overtopping volume can be obtained from Equation 13:

$$\delta_{V_{ot}} = k \delta_{V_l} \quad (13)$$

where, $\delta_{V_{ot}}$ represents uncertainty in overtopping volume, δ_{V_l} represents uncertainty of initial mass volume, including uncertainty of glacier avalanche δ_{V_g} and uncertainty of deformed slope δ_{V_l} . Finally, we used Froehlich's equations (Froehlich, 1995) to obtain uncertainties of dam breach discharge (δ_{Q_p}) and dam failure time (δ_{T_f}):

$$\begin{cases} \delta_{Q_p} = 0.607(r \delta_{V_{ot}})^{0.295} (d_1)^{1.24} \\ \delta_{T_f} = 0.00254(r \delta_{V_{ot}})^{0.53} (d_2)^{-0.9} \end{cases} \quad (14)$$

where r is an empirical coefficient, usually greater than 1. d_1 and d_2 represent the height of dam breach and the water level above the final bottom, which are derived from dam height and lake depth. However, GLOF processes exhibit inherent sensitivity to model parameters and the change of the lake and its surrounding conditions. Additionally, uncertainties in failure triggers, magnitudes, and mechanisms propagate to flood simulation results (Sattar et al., 2023). Given the challenges in quantifying these parameters, we characterized flooding process uncertainties by calculating the standard deviation of modeled discharge and depth in grid cells surrounding three villages (Kohanpur et al., 2023).

4. Results

4.1. Glacial Lake and Volume Changes

We analyzed Landsat-based optical images to document the evolution of Jiongpu Co from 2000 to 2024. Figure 5 shows the expansion of the glacial lake area. The lake had expanded southeasterly toward the source of its parent glacier tongue, doubling in size over the past 25 years. Then, we calculated the area and volume change in winter from 1990 to 2024, considering the seasonal meltwater change in the same season (Figure 6). The lake area in 1999 was estimated to be $2.41 \pm 0.17 \text{ km}^2$, based on inventory data from the TPDC (X. Wang et al., 2020). By the winter of 2002, Jiongpu Co had expanded to $2.64 \pm 0.19 \text{ km}^2$ and the volume was 0.18 km^3 . During 2002–2018,

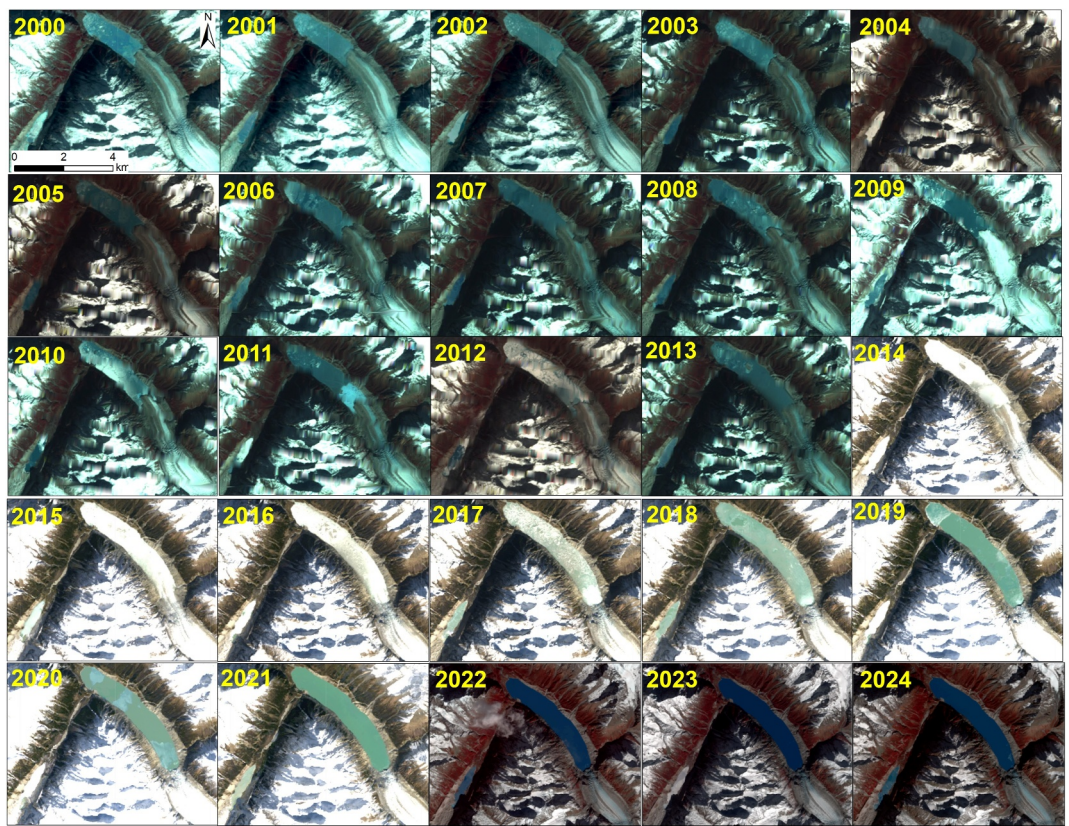


Figure 5. Lake development and expansion of Jiongpu Co from 2000 to 2024.

the lake expanded from $2.76 \pm 0.12 \text{ km}^2$ to $5.34 \pm 0.14 \text{ km}^2$, at an average rate of $0.16 \text{ km}^2/\text{year}$. Then, the area of Jiongpu Co grew slowly from 2019 to 2024. Finally, the lake area expanded to $5.31 \pm 0.20 \text{ km}^2$ in 2024, suggesting that the area had more than doubled since 1999. The lake volume grew to 0.44 km^3 in 2024 (Figure 6).

4.2. Glacier 3-D Flow Velocities and Displacement Time Series

The 3-D glacier flow velocities from January 2019 to December 2021 were derived using the PO-MSBAS method. Due to discontinuities of the descending SAR image, we divided the velocity measurements into different phases, as shown in Figure 7. The color represents the vertical velocity while the arrow represents the horizontal velocity. The horizontal flow velocity from 29 January 2019 to 30 April 2019 reached a maximum of 150 cm/day (Figure 7a). The maximum vertical upward velocity reached 43 cm/day, occurring at the western

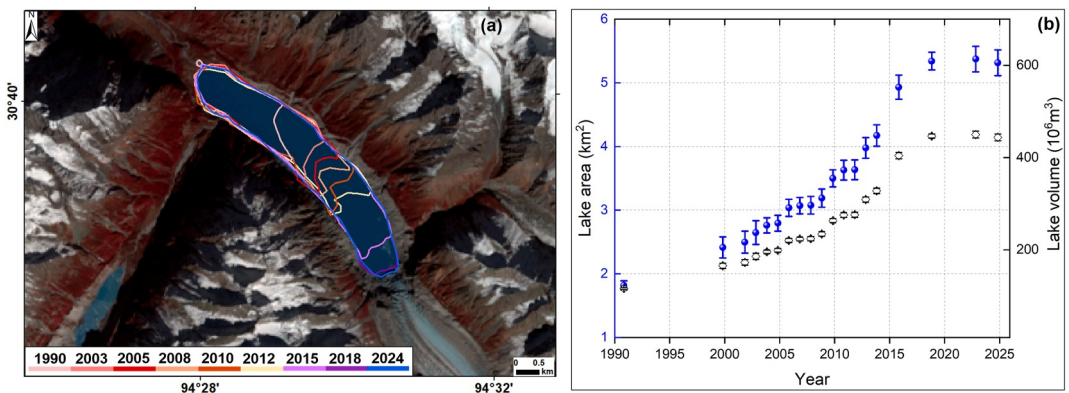


Figure 6. Area and volume expansion of Jiongpu Co from 1990 to 2024.

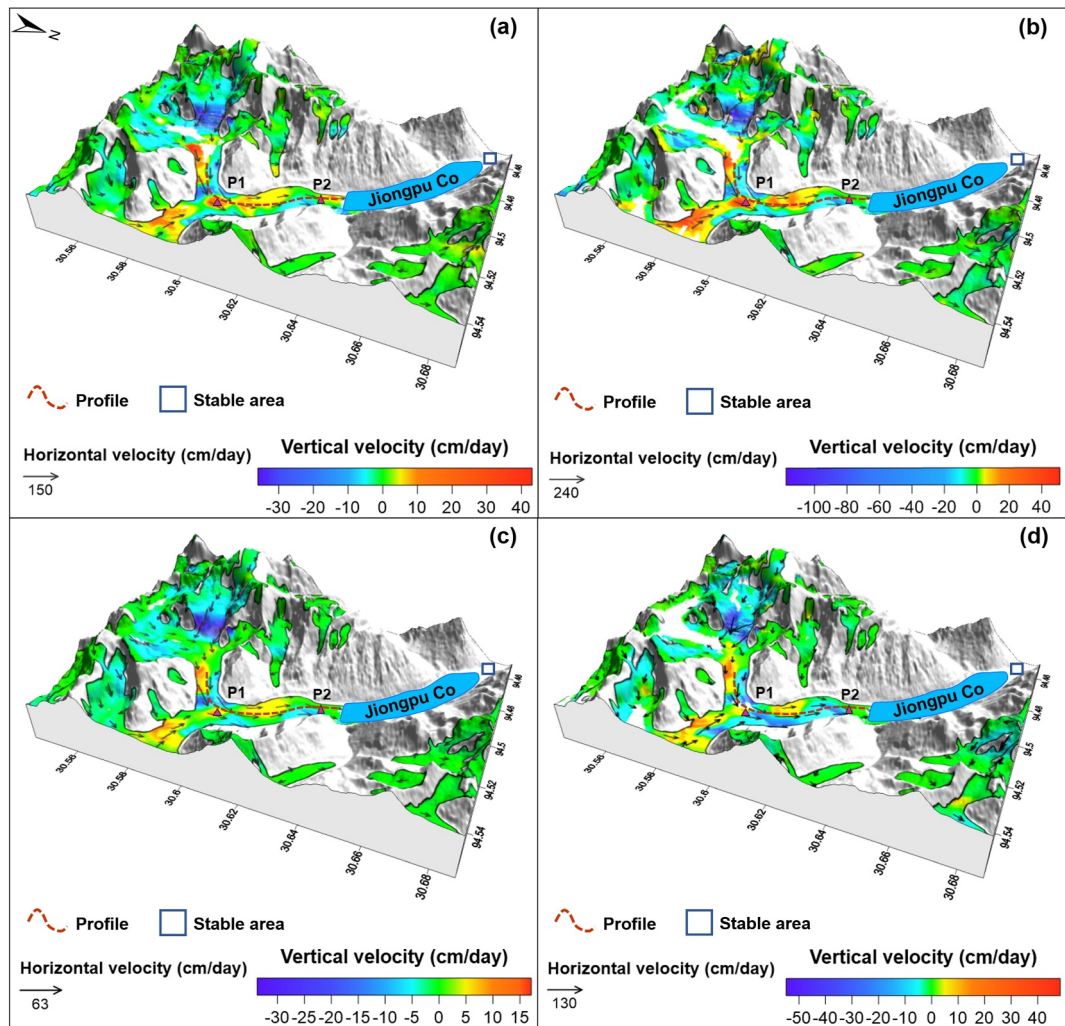


Figure 7. 3-D glacier velocities at different periods. (a)–(d) 3-D glacier velocities from 29 January 2019 to 30 April 2019, 13 November 2019 to 17 July 2020, 18 January 2021 to 26 March 2021, 10 August 2021 to 15 December 2021, respectively.

tributary confluence with the main trunk. The maximum vertical downward flow velocities were large 36 cm/day. Figure 7b shows the 3-D velocities from 13 November 2019 to 17 July 2020. The maximum horizontal velocity reached 240 cm/day, which occurred at the confluence of the western tributary with the main trunk. The maximum upward velocity occurred at the main tributary at 51 cm/day. The maximum downward velocity of 118 cm/day occurred at the peak of the western tributary. Figure 7c shows the 3-D glacier flow velocities from 18 January 2021 to 26 March 2021, with a maximum flow rate of 63 cm/day horizontally. The downward glacier motion occurred at the peak of the western tributary with a flow rate of 34 cm/day. The maximum upward flow velocity was 17 cm/day. From 10 August 2021 and 15 December 2021, the glacier arrived at a maximum horizontal velocity of 130 cm/day, as shown in Figure 7d. The maximum downward vertical velocity during this period got to 55 cm/day. The maximum upward flow velocity was 49 cm/day.

To clearly demonstrate the temporal variations in velocity, we obtained 3-D glacier displacement time series at two selected points (Figure 8). P1 is located at the confluence of the western tributary with the main trunk while P2 is near Jiongpu Co (Figure 7). We connected the displacement time series from 2019 to 2021. P1 exhibited northward motion in the north-south direction, with a cumulative displacement of 594.7 ± 3.7 m. The western motion displaced at 223.8 ± 1.0 m. The cumulative upward displacement reached 75 ± 0.7 m in the vertical direction during 2019–2021. For P2, the cumulative displacement in the north-south, east-west, and vertical directions came to 302.4 ± 2.5 m, 140.9 ± 0.9 m, and 128.3 ± 0.8 m, respectively. At P1 and P2, the glacier

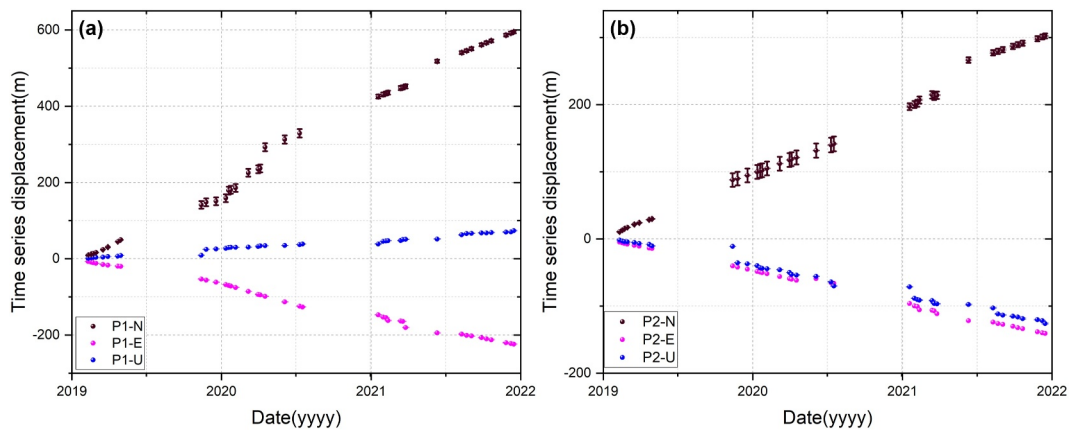


Figure 8. 3-D displacement time series of the parent glacier at P1 (a) and P2 (b) from 2019 to 2021. Error bars, derived from a stable region, indicate STD values of glacier time-series displacements.

exhibited northwesterly movement in the horizontal direction. However, the glacier revealed different motions in the vertical direction, in which P1 experienced upward motion and P2 showed downward motion. Moreover, the cumulative downward displacement at P2 is greater than the upward displacement at P1. The difference in the vertical motion is influenced by local topographic variations and the proglacial lake (Carrivick & Tweed, 2013; Emmer, 2017).

4.3. Glacier Thickness and Potential Avalanche Volume

The thickness of glaciers from our approach depends on the selection of the rheological parameter, which acts as a scaling factor. Thus, we based the rheological parameter on the ratio of the glacier slope to the surface velocity. Figure 9 shows the significant output for choosing the optimum rheological parameter. First, we estimated average horizontal velocity by combining the north-south and east-west velocities from the result of 3-D glacier velocities, as shown in Figure 9a. The averaged horizontal velocity shows that the maximum horizontal motion occurred at the confluence of the western tributary with the main trunk, reaching 272 m/yr. The surface slope was obtained from the resampled SRTM DEM provided by ALOS PALSAR radiometric terrain corrected (RTC) products. Figure 9b exhibits that the glacier features a local average slope angle of 10°. Then, we determined the ratio of the slope to the surface velocity, which is less than 0.01. Especially, most of the ratio value is distributed within 0.002 (Figure 9c). Finally, we retrieved the optimum rheological parameter based on the calculated ratio. Figure 9d shows the spatial distribution of the rheological parameter rather than a single or empirical value for the entire glacier. The result indicates that the glacier moves fast on its surface and slow at the base (Delbridge et al., 2016; Millan et al., 2022; Morlighem et al., 2011).

Therefore, we derived the optimum glacier thickness in our study based on the updated optimum rheological parameter, as shown in Figure 10a. It is worth noting that the inversion thickness is associated with SAR-derived 3-D flow velocities, for which there is a lack of data due to the absence of 3D flow velocities. We identified the potential avalanche zone of the slope $>14^\circ$, as shown in the red area in Figure 10b. We then combined the optimum glacier thickness and the criterion slope $>14^\circ$ to derive the volume of the potential glacier avalanche. The volume of the potential avalanche zone is $1.8 \pm 0.06 \times 10^8 \text{ m}^3$.

4.4. Slope Deformation and Potential Landslide Volume

Slope deformation acts as a direct instability indicator (Rounce et al., 2016). We monitored the deformation rate and time series on the surrounding slopes above Jiongpu Co based on the MTI method. The LOS deformation rate at the surrounding slopes in Figure 11a shows that the western slope deformed with the highest deformation rate of 200 mm/yr. We then focused on measurement points at the head (H1-H2), middle (M1-M2), and toe (T1-T2) part of the western slope to understand its kinematic behavior. Figure 11b presents the deformation time series at these six points on the western slope. The head of the slope (H1-H2) was identified as the most active region, with

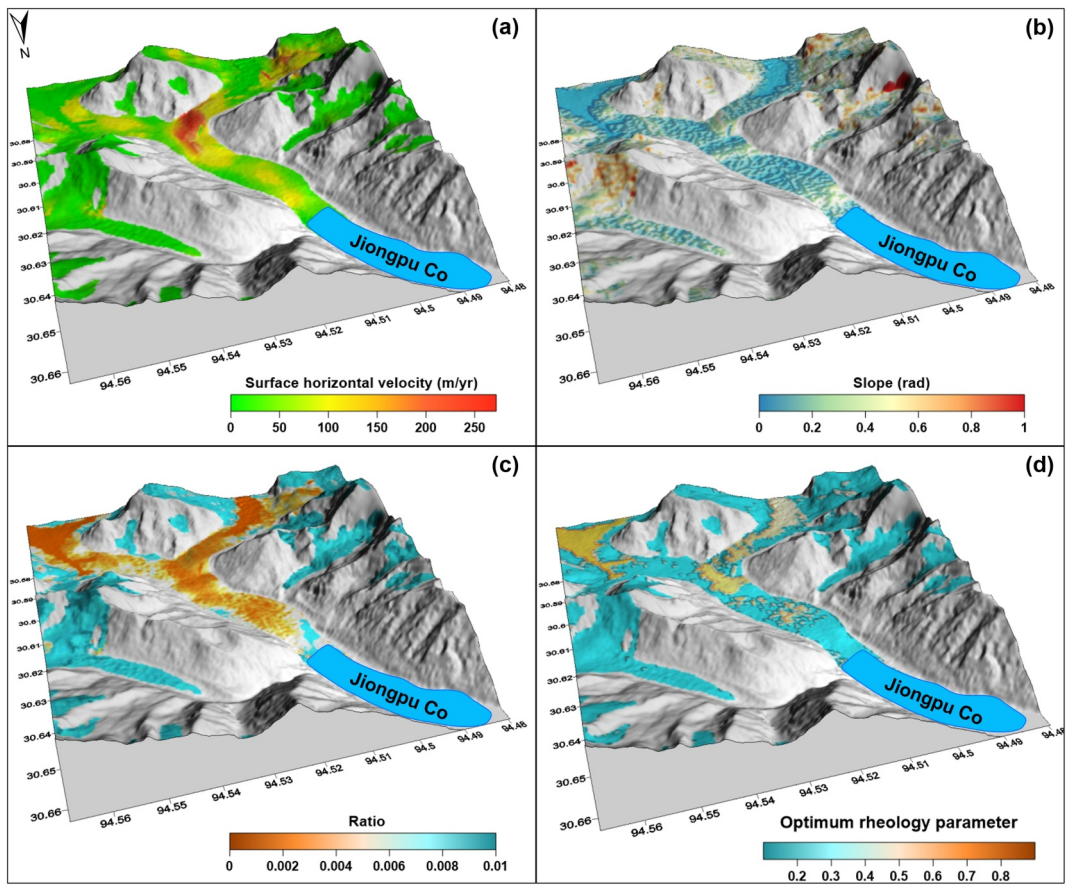


Figure 9. Choice of rheological parameter. (a) Surface flow velocity of the glacier (units: m/yr). (b) Slope of the glacier (units: radian). (c) Ratio of the slope and surface velocity. (d) Rheological parameter.

cumulative deformation of 258.4 ± 1.6 mm and 212.1 ± 10 mm, respectively. At the middle of the slope, the cumulative deformation arrived at 198.6 ± 11 mm and 176.4 ± 0.1 mm at points M1 and M2, respectively. The toe of the slope (T1-T2) presented the smaller deformation, showing the cumulative deformation was 130.1 ± 2.3 mm and 134.0 ± 2.0 mm, respectively.

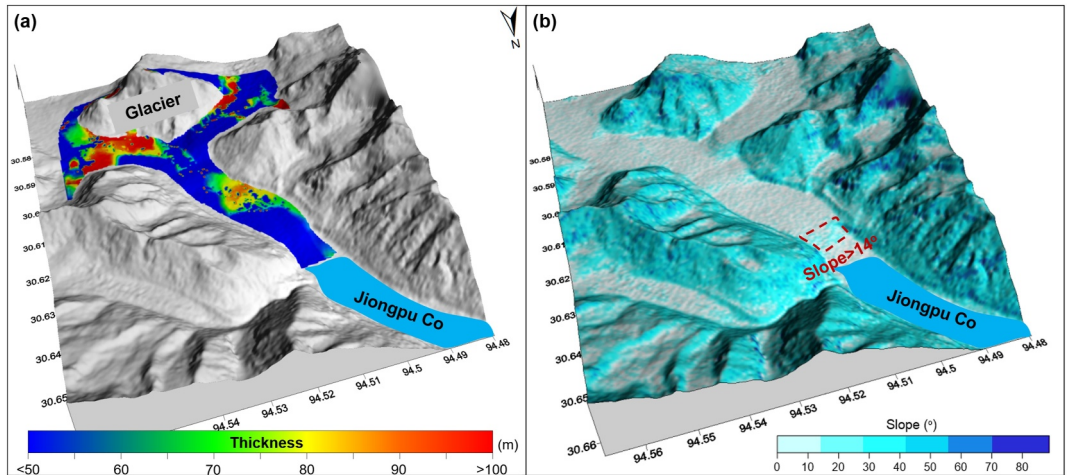


Figure 10. Glacier thickness and the topographic slope. The red area represents the potential avalanche zone with a slope angle $>14^\circ$. (a) Glacier thickness result. (b) Topographic slope of the parent glacier.

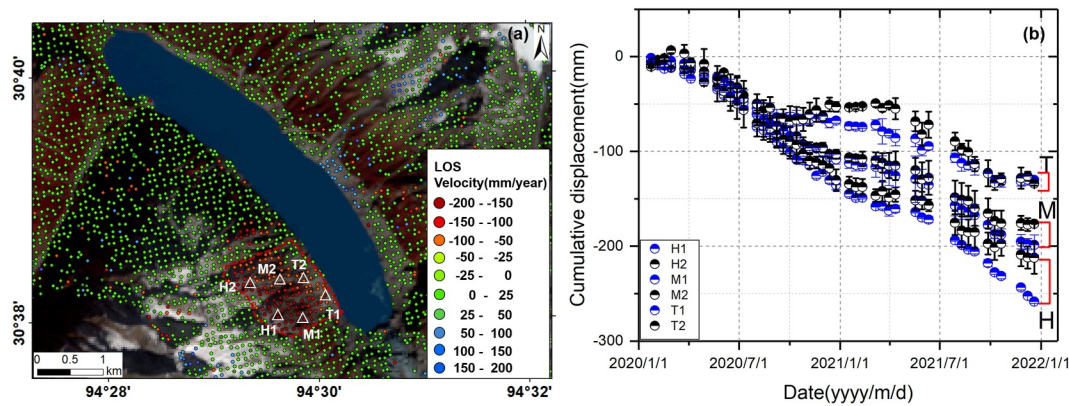


Figure 11. Deformation rate and time series on the surrounding slopes above Jiongpu Co. (a) LOS deformation rate during 2019–2021. (b) Deformation time series at six points on the western slope. Error bars, derived from a stable region, indicate the STD values of slope deformation time series.

The unstable western slope exhibited a distinct deformation zone. Subsequently, we estimated the area of the potential landslide using the monitored deformation zone, as shown in the red dotted area in Figure 11a. We further obtained the volume based on Equation 8, which is validated for landslide volume estimation in mountainous regions (Korup, 2006). The volume of this potential landslide above Jiongpu Co was $3.5 \pm 0.2 \times 10^8 \text{ m}^3$.

4.5. GLOF Process Modeling

We modeled the GLOF process of Jiongpu Co under two different scenarios, including glacier avalanche and landslide runoff into the lake. The obtained overtopping volumes are $1.94 \pm 0.1 \times 10^7 \text{ m}^3$ and $9.89 \pm 0.6 \times 10^7 \text{ m}^3$, respectively, based on Equations 9 and 10. Figure 12 presents the maximum flow depths and dam discharges of the GLOF process through these two different scenarios. The potential glacier avalanche into the lake leads to a maximum flooding depth of 32 m (Figure 12a). GLOF caused by landslide runout into the lake reaches a maximum depth of 43 m (Figure 12b). The flood discharge at the breached dam originating from the glacier avalanche takes 95 ± 8 min to reach a maximum discharge of $\sim 6,408 \pm 352 \text{ m}^3/\text{s}$. The maximum discharge at the dam caused by landslide runout into the lake is $29,011 \pm 1063 \text{ m}^3/\text{s}$ in 150 ± 43 min.

We further evaluated the downstream flooding process including Jinlingcun (village 1), Jitangcun (village 2), and Jiecun (village 3), as presented in Figure 13a. The distance from Jiongpu Co to the three villages is 12, 1, and 26 km, respectively. Figure 13 and Table 2 show the GLOF outflow depth and discharge at these three villages with two varied outburst scenarios. The GLOF hazard of Jiongpu Co reveals that potential impact from glacier avalanche into the lake produces a peak discharge of $6,388 \pm 130 \text{ m}^3/\text{s}$ at village 1. The maximum simulated flow depth reaches 7.2 ± 1 m at 650 min (Figure 13b). However, when a landslide potentially falls into the lake, the peak discharge surges to $20,902 \pm 201 \text{ m}^3/\text{s}$. The maximum flow depth is 10.9 ± 1 m at 300 min at downstream village 1 (Figure 13b). The GLOF peak is $6,281 \pm 47 \text{ m}^3/\text{s}$ at village 2 under the potential glacier avalanche into the lake. The maximum flow depth gets to 7.0 ± 1 m at 700 min (Figure 13c). For the landslide impacting the lake, the peak discharge is up to $17,115 \pm 236 \text{ m}^3/\text{s}$, with a maximum depth of 10.7 ± 1 m at 350 min (Figure 13c). At village 3, the peak discharge caused by a potential glacier avalanche into the lake reduces to $6,094 \pm 188 \text{ m}^3/\text{s}$, accompanying the maximum flow depth of 6.6 ± 0.2 m at 750 min (Figure 13d). In the case where a landslide moves into the lake, the GLOF produces a maximum discharge of $13,948 \pm 1291 \text{ m}^3/\text{s}$. The maximum simulated flow depth reaches 10.2 ± 0.5 m at 450 min at village 3 (Figure 13d).

5. Discussion

GLOFs triggered by cascading mass movements—such as glacial avalanches or landslides into lakes—are increasingly recognized as compound hazards in high-mountain regions. However, the lack of high-resolution observations of glacier dynamics and slope instability often hinders the identification of GLOF precursors and the simulation of hazard cascades. Jiongpu Co serves as a critical case study due to its rapidly expanding lake area, adjacent unstable slopes, and retreating glaciers—factors that collectively heighten multi-hazard risks. In this

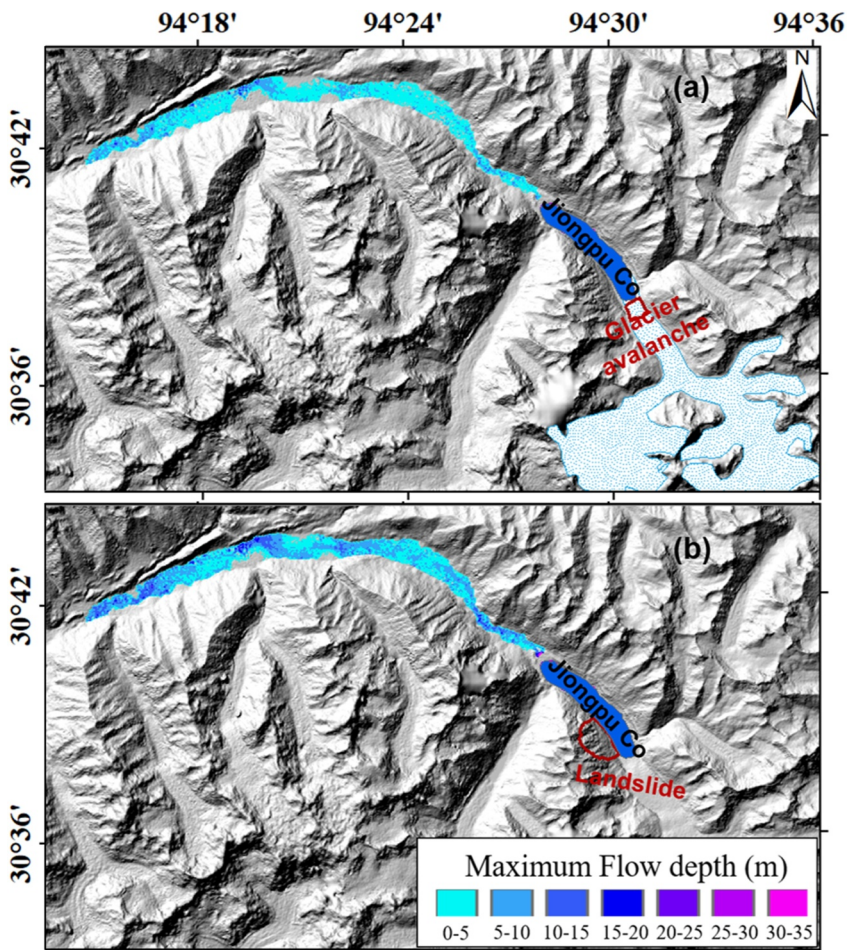


Figure 12. Maximum flow depth under two GLOF process scenarios. (a) Glacier avalanche into the lake. (b) Landslide runout into the lake.

section, we discuss key findings related to glacier motion, slope deformation, GLOF exposure, and associated uncertainties to advance our understanding of GLOF initiation and propagation mechanisms.

5.1. Dynamics of 3-D Flow Velocities During Different Periods

We obtained the 3-D velocities and displacement time series, which provide insights into the glacier dynamics and aid in identifying potential triggers of GLOF hazards (D. Li et al., 2022; Peng et al., 2023). To further investigate spatial variations in 3-D glacier velocities across different periods, we extracted 3-D velocity time series along the profile shown as a red curve in Figure 7.

Figures 14a–14d present north-south glacier flow velocity time series across four periods, revealing significant temporal fluctuations in northerly motion. Spatially heterogeneous flow velocities were observed: From 29 January 2019 to 30 April 2019 (Figure 14a), a spring season, cumulative maximum flow velocity was as high as 87 cm/day at ~1.6 km. The northward velocity began to surge on 23 April 2019. From 13 November 2019 to 17 July 2020 (Figure 14b), the maximum northward velocity reached 197 cm/day at ~1.8 km. A significant increase in northward flow velocity was observed on 4 June 2020. Between 18 January 2021 and 26 March 2021 (Figure 14c), the cumulative northward velocity reached 46 cm/day at ~1.1 km. On 14 March 2021, the northward flow velocity increased significantly. From 10 August 2021 to 15 December 2021 (Figure 14d), the cumulative velocity was up to 84 cm/day at 2.8 km, illustrating variation in flow velocity at greater distances. The northward flow velocity accelerated significantly on 26 November 2021. Figure 14e displays averaged north-south velocities across the four periods overlaid with elevation data (0–6 km profile). The differences in the

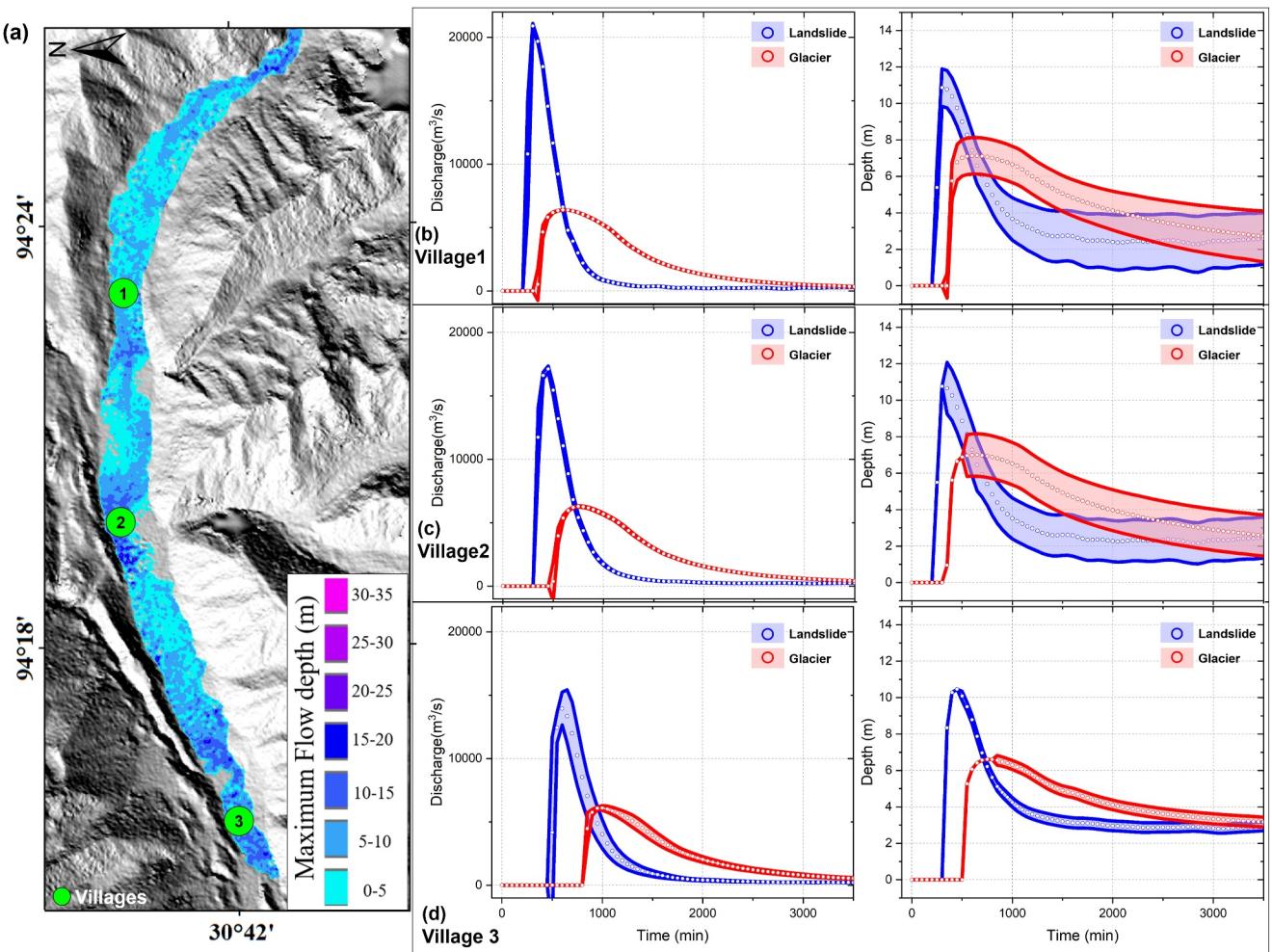


Figure 13. Flood discharge and depth of Jiongpu Co at three downstream villages. (a) Maximum flow depth caused by landslide into the lake and locations of three villages. (b)–(d) Discharge and flow depth at downstream villages 1, 2, and 3, respectively.

averaged northward flow velocity show that the highest velocity happened in the period from 29 January to 30 April 2019. The elevation appears to decrease gradually from ~4,880 to ~4,118 m. At steep terrain with rapid elevation changes, from 4,805 m at about 0.8 km–4,619 m at 1.6 km, there is a tendency for the flow velocity to accelerate, indicating the influence of gravitational forces on glacier movement (Benn et al., 2007; Jiskoot, 2011).

Figure 15 presents detailed time series and averaged velocities of glacier flow dynamics across four periods. Spatially, eastward motion occurs within 1.8 km of the profile, beyond which the glacier transitions to westward flow consistent with its geometric orientation. From 29 January 2019 to 30 April 2019 (Figure 15a), in spring, the

Table 2
GLOF Peak Discharges and Flow Depths at Three Downstream Villages Under Two Different Scenarios

Scenarios	Routing location	Time (min)	Discharge (m³/s)	Flow depth (m)
Glacier avalanche into the lake	Village 1	650	$6,388 \pm 130$	7.2 ± 1
	Village 2	700	$6,281 \pm 47$	7.0 ± 1
	Village 3	750	$6,094 \pm 188$	6.6 ± 0.2
Landslide runout into the lake	Village 1	300	$20,902 \pm 201$	10.9 ± 1
	Village 2	350	$17,115 \pm 236$	10.7 ± 1
	Village 3	450	$13,948 \pm 1291$	10.2 ± 0.5

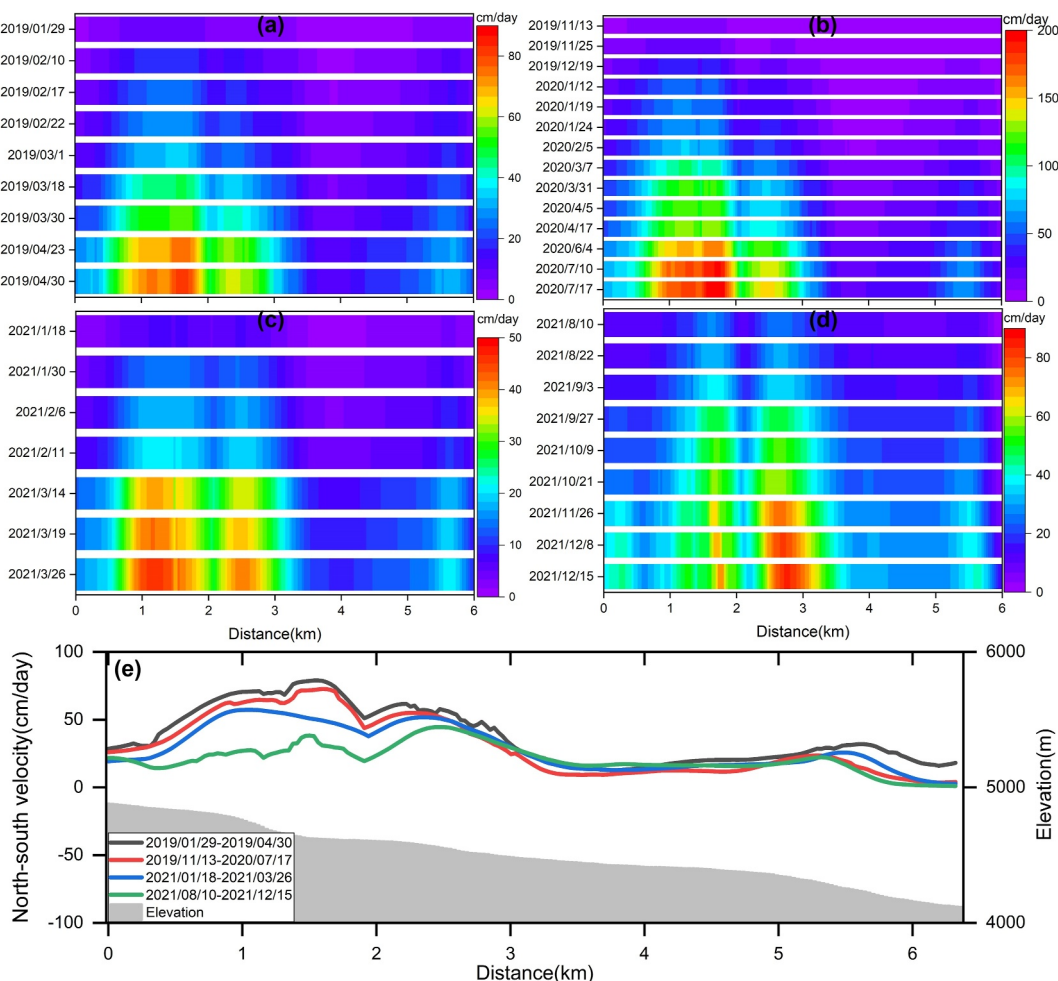


Figure 14. Temporal evolution of north-south glacier velocity on profile, represented in Figure 7, during four different periods. (a)–(d) Velocity time series in north-south direction during the period of 2019/1/29–2019/4/30; 2020/11/13–2020/7/17; 2021/1/18–2021/3/26; and 2021/8/10–2021/12/15, respectively. (e) Averaged north-south velocity and elevation.

cumulative maximum velocity at ~ 1.1 km was as high as 80 cm/day. The eastward velocity surged from 30 March 2019. The western maximum velocity was 23 cm/day. Figure 15b shows the flow velocity in the east-west direction from 10 August 2021 to 15 December 2021, indicating a maximum eastern velocity of 158 cm/day at ~ 1 km. The obvious increase in glacier dynamics happened from 4 June 2020. Between 18 January 2021 and 26 March 2021 (Figure 15c), the maximum eastern velocity happened at ~ 1.1 km with 43 cm/day. The glacier dynamic significantly increased on 14 March 2021. Figure 15d presents the time series glacier velocity from 10 August 2021 to 15 December 2021. The result displays the glacier's maximum eastern velocity of up to 68 cm/day at the beginning of the profile, which suggests spatial heterogeneity in glacier movement. Figure 15e displays averaged east-west velocities across the four periods, overlaid with elevation data. The highest eastward velocity occurred in the period from 29 January 2019 to 30 April 2019. Steep topographic gradients correlate with increased flow velocity variations, indicating a relationship between elevation and flow dynamics (Samsonov et al., 2021; Zekollari et al., 2022).

Figure 16 presents vertical velocity time series across different periods, revealing spatial variations along the profile. From 29 January 2019 to 30 April 2019 (Figure 16a), the maximum downward motion happened at ~ 1.3 km of 13 cm/day, while the maximum upward motion occurred at ~ 1.8 km of 22 cm/day. The vertical velocity began to significantly increase on 23 April 2019. Figure 16b shows the vertical time series velocity from 13 November 2019 to 17 July 2020. The downward maximum velocity reached -38 cm/day at ~ 1.1 km. The upward maximum velocity was 37 cm/day at ~ 1.9 km (Figure 16b). During the period from 18 January 2021–26

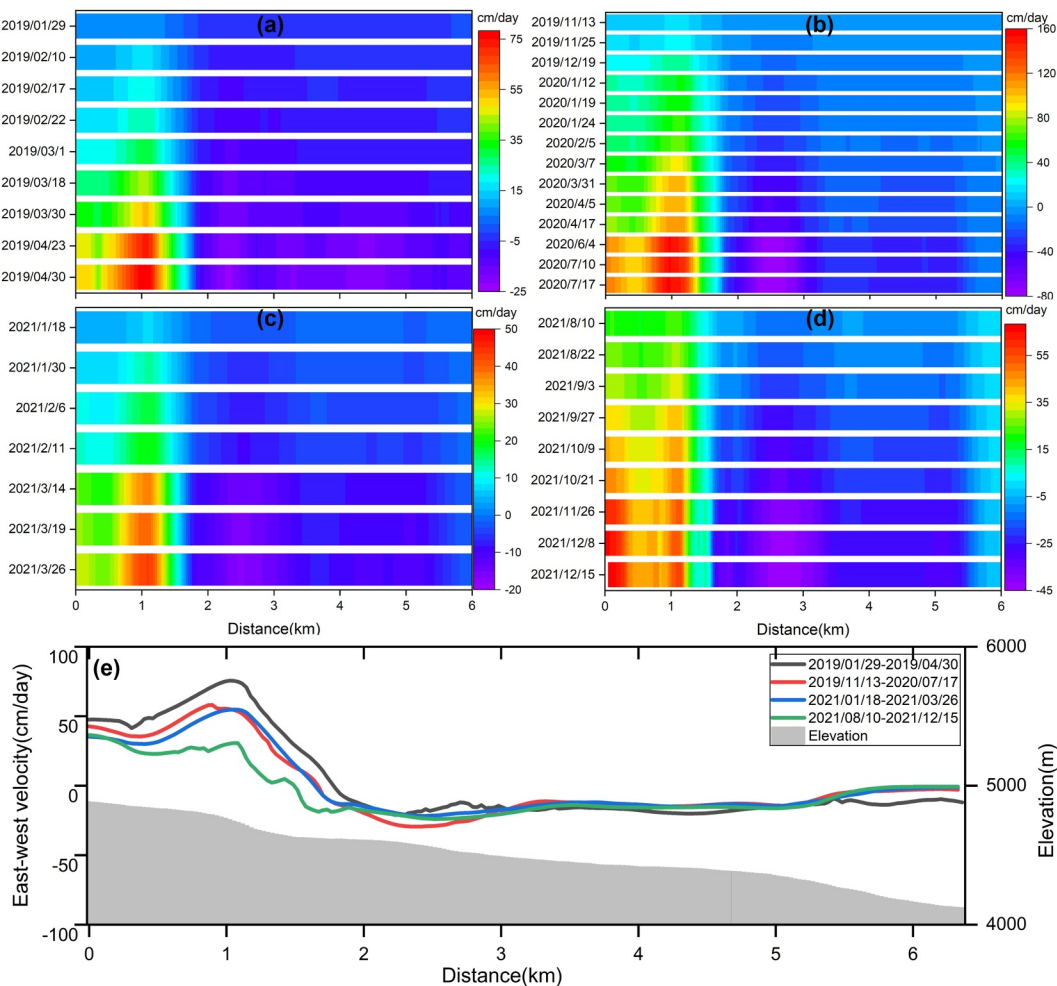


Figure 15. Temporal evolution of east-west glacier velocity on profile, represented in Figure 7, during four different periods. (a)–(d) Velocity time series in east-west direction during the period of 2019/1/29–2019/4/30; 2020/11/13–2020/7/17; 2021/1/18–2021/3/26; and 2021/8/10–2021/12/15, respectively. (e) Averaged east-west velocity and elevation.

March 2021 (Figure 16c), vertical velocity experienced upward-downward-upward-downward motion. The downward maximum velocity reached -11 cm/day at $\sim 1.4 \text{ km}$. The upward maximum velocity was 13 cm/day at the beginning of this profile. In the period from 10 August 2021 to 15 December 2021 (Figure 16d), the vertical motion shows its complex change. The averaged vertical velocity along the elevation is exhibited in Figure 16e. Similarly, the highest vertical velocity happened in the period from 29 January 2019–30 April 2019.

Temporally, 3-D glacier flow velocities averaged highest during spring 2019. Spatially, horizontal velocities were primarily influenced by topography, with acceleration occurring at steep elevation gradients. Vertical velocities exhibited complex patterns correlated with glacier mass balance variations (Zekollari et al., 2022; Zhang et al., 2023). These observed variations highlight the necessity of continuous monitoring to understand the mechanisms driving glacier dynamics and their relationship to GLOF hazards.

5.2. Climatic Effect on Slope Deformation Above Jiongpu Co

The magnitude and frequency of slope instability in alpine regions have increased in recent decades (S. K. Allen et al., 2011; Coe et al., 2018; Gariano & Guzzetti, 2016; Savi et al., 2021; Stoffel & Huggel, 2012; Stoffel et al., 2024) and are projected to intensify further, posing growing risks to expanding populations and infrastructure (Hock et al., 2019). In our study, we identified slope instability above the glacial lake and monitored its deformation time series (Figure 11). To investigate climatic influences on slope movement, seasonal deformation was derived by removing linear trends from the time series (Hu et al., 2018, 2019). Daily precipitation data were

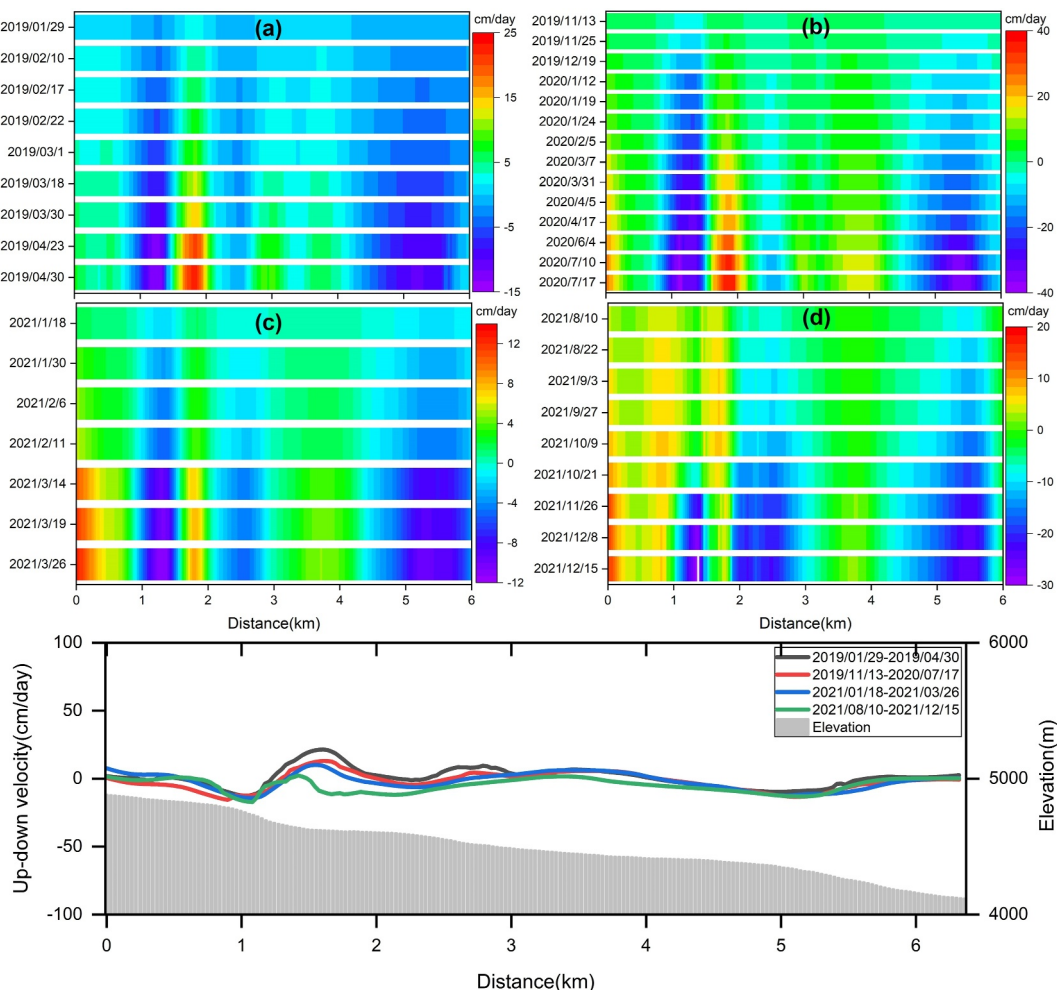


Figure 16. Temporal evolution of vertical glacier velocity on profile, represented in Figure 7, during four different periods. (a)–(d) Velocity time series in the vertical direction during the period of 2019/1/29–2019/4/30; 2020/11/13–2020/7/17; 2021/1/18–2021/3/26; and 2021/8/10–2021/12/15, respectively. (e) Averaged vertical velocity and elevation.

obtained from GPM (<https://gpm.nasa.gov/data/directory>; Skofronick et al., 2017), and daily temperature records were collected from a weather website (<https://lishi.tianqi.com/bomi/index.html>).

Figure 17a shows averaged seasonal deformation at the head, middle, and toe regions of the western slope, alongside daily temperature and precipitation. The results reveal periodic variations in seasonal slope deformation (spherical markers), daily temperature (blue dots), and precipitation (gray bars) over approximately 1 year. Seasonal deformation changed from -14 to 24 mm, -18 to 12 mm, and -26 to 12 mm at the head, middle, and toe parts of the western slope, respectively. Temperature increased from January to June, followed by decreases from July to December. Also, the daily precipitation exhibited seasonal patterns, with higher precipitation occurring during warmer summer months.

To understand correlations between seasonal deformation and climatic factors across slope segments, cross-correlation analysis was performed (Figures 17b and 17c). The results indicate temporal relationships between seasonal deformation and temperature. The head region exhibited a maximum positive correlation ($r = 0.59$) with temperature at a 63-day lag, while the middle region reached a moderate correlation ($r = 0.52$) at a 92-day lag. In contrast, the toe region displayed a strong negative correlation ($r = -0.73$) at a 53-day lag, indicating that temperature exerts a significant influence on toe deformation. Precipitation correlations were generally weak ($r < 0.35$), as shown in Figure 17c. These results highlight temperature as a key driver of seasonal slope dynamics, particularly at the toe. It is important to note that while cross-correlation identifies temporal associations, it does

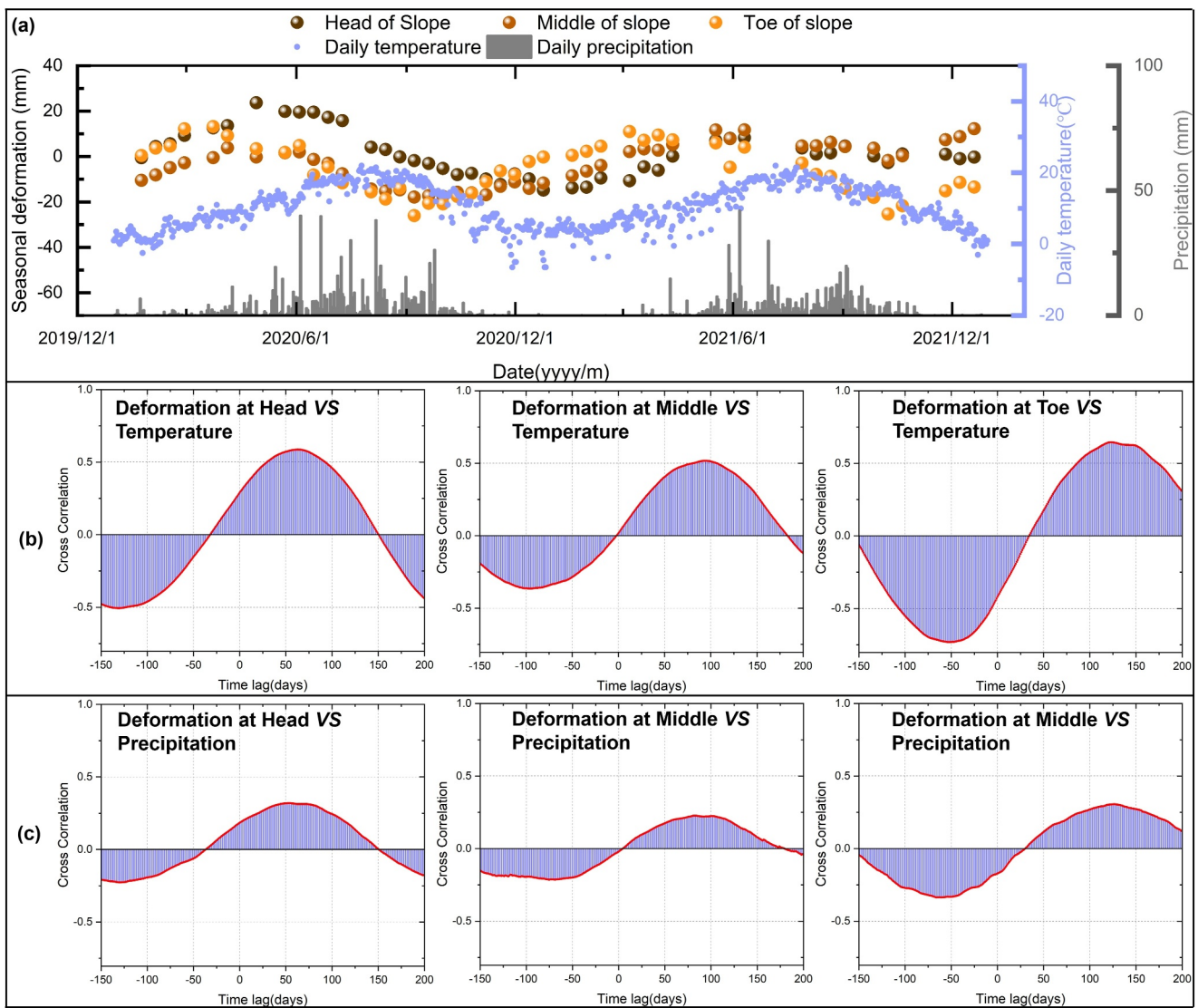


Figure 17. Climatic analysis of periodic components in deformation time series of the western slope. (a) Seasonal deformation time series at the different sections of the slope, daily temperature, and daily precipitation. (b) Cross-correlation between seasonal slope deformation at different parts and temperature. (c) Cross-correlation between seasonal slope deformation at different parts and precipitation.

not establish causation due to potential confounding variables. Factors such as snowmelt infiltration (Iverson, 2000), freeze-thaw action (Matsuoka & Murton, 2008), and groundwater fluctuation (van Asch et al., 1999) may also influence slope deformation (Pánek & Klimeš, 2016).

This study establishes relationships between landslide deformation and climatic factors, particularly temperature. The findings highlight the importance of ongoing monitoring to predict landslide dynamics and assess climate change impacts on slope stability. Understanding these dynamics is critical for implementing effective GLOF risk management and mitigation strategies in HMA regions (D. Li et al., 2022; Sattar et al., 2023).

5.3. Avalanche-Induced and Landslide-Induced GLOF Exposure

The GLOF flooding depths and discharges at three downstream villages were evaluated under two scenarios in Section 4.5. To further characterize GLOF intensity and hazard risk, we obtained the high-intensity GLOF (flow depth > 1 m) and moderate GLOF intensity (flow depth < 1 m) (S. Allen et al., 2017) under glacier avalanche and landslide scenarios. Figure 18 illustrates GLOF intensity spatial distribution. We found that landslide-induced GLOFs exhibit a larger high-intensity inundation area compared with glacier avalanche scenarios. This

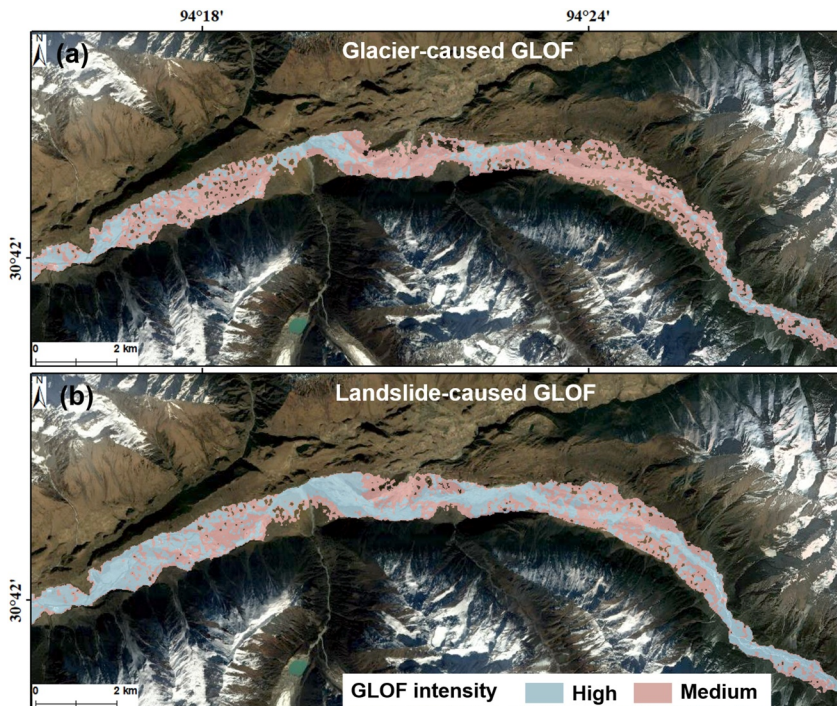


Figure 18. Zones of high (flooding depth > 1 m) and medium (flooding depth < 1 m) GLOF intensity under glacier-avalanche-induced GLOF (a) and landslide-induced GLOF (b).

discrepancy is attributed to differences in initial source volume and overtopping volume (X. Lu et al., 2022). Varying flood intensities underscore the necessity of ongoing deformation monitoring in surrounding areas and trigger analysis for effective GLOF hazard prevention.

Notably, expanding glacial lakes in HMA regions coincide with expanding infrastructure development. This is exemplified in the Jiongpu area, where downstream villages have seen urban and agricultural expansion over 17 years (Figure 19). All villages exhibit new construction, underscoring long-term urban growth trends. Given the escalating glacier-related hazards in the Himalayas, comprehensive assessments are critical to identify infrastructure and communities at risk. These include identifying potential glacier avalanches and slopes insatiably, quantifying potential failure volumes, and simulating GLOF scenarios (e.g., Sattar et al., 2023; L. Yang et al., 2023). Continued interdisciplinary research and regional collaboration are essential for developing tailored risk management frameworks addressing Himalayan-specific challenges (Sattar et al., 2022).

5.4. Uncertainties and Future Directions

The uncertainties in modeled GLOF processes originate from multiple sources, including initial mass movements, lake bottom topography, and model parameters (Sattar et al., 2023). A key challenge in quantifying GLOF uncertainty lies in constructing realistic process-chain scenarios for predictive modeling (Emmer, 2017). The important source of uncertainty is the initial mass movement source zone and its volume. In our study, we identified glacier avalanche source zones using topographic slope criteria (S. K. Allen et al., 2019). To define the magnitude of initial avalanche zones, we derived glacier thickness from multi-track SAR data sets, with uncertainty analyzed via Equation 12. Figure 20 shows the STD of glacier thickness. The thickness uncertainty is mainly distributed in the glacier boundary regions with a maximum value of ~5 m. The average standard deviation is 0.14 m. Hence, we obtained the volume and its uncertainty of potential glacier avalanche with $1.8 \pm 0.06 \times 10^8 \text{ m}^3$. For potential slope movement into the lake, we identified the initial slope source zones using the InSAR method. The uncertainties of slope deformation were estimated, as shown in Figure 11. We obtained a landslide volume of $3.5 \pm 0.2 \times 10^8 \text{ m}^3$. Then, the overtopping volume and its uncertainties for both scenarios were retrieved based on Equations 9, 10 and 13. The overtopping volumes are $1.94 \pm 0.1 \times 10^7 \text{ m}^3$ and $9.89 \pm 0.6 \times 10^7 \text{ m}^3$, respectively.

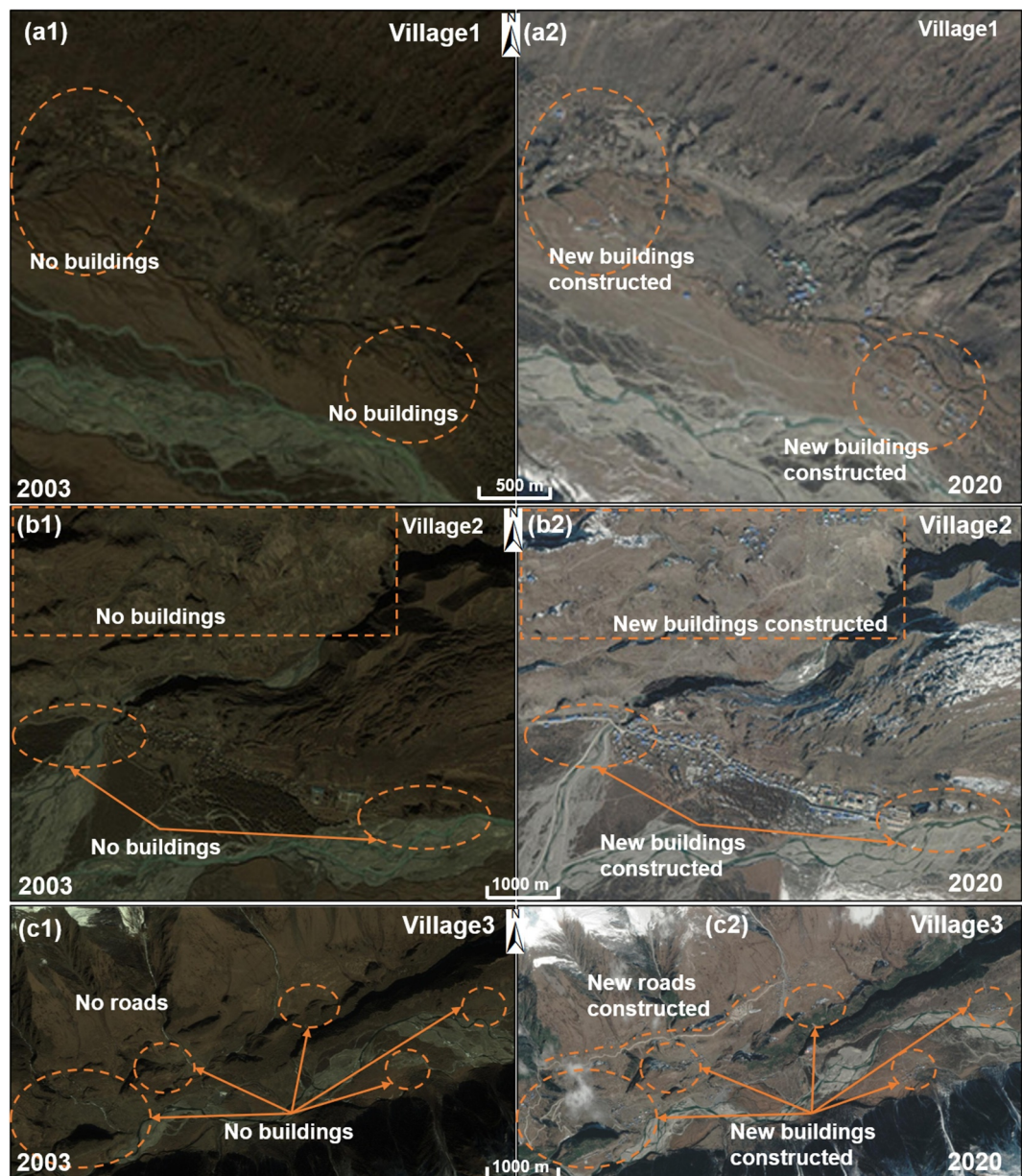


Figure 19. Changes in the three downstream villages in the last 17 years from Google Earth images (a) village 1, (b) village 2, and (c) village 3.

Based on dam breach hydrology from previous works (Froehlich, 1995), we calculated the flooding uncertainties at the breached dam based on Equation 14 and analyzed them in Section 4.5. Froehlich's empirical relationships, derived from historical failures of embankment dams, provide a simplified method for estimating breach parameters. These relationships are compatible with the conceptual embankment geometry used in our HEC-RAS-based dam breach model, which focuses on simulating the downstream flood propagation. GLOF processes are inherently influenced by model parameters, including basal friction angle, phase change-induced flow transitions, and released solid content (Sattar et al., 2023). Model inputs were constrained by previous GLOF process-chain studies (Sattar et al., 2023; L. Yang et al., 2023). However, parameterizations derived from limited GLOF simulations introduce quantifiable uncertainties. Therefore, to characterize uncertainties in GLOF results, standard deviations of discharge and depth were calculated in neighboring grid cells at downstream villages, as shown in Figure 13 and Table 2.

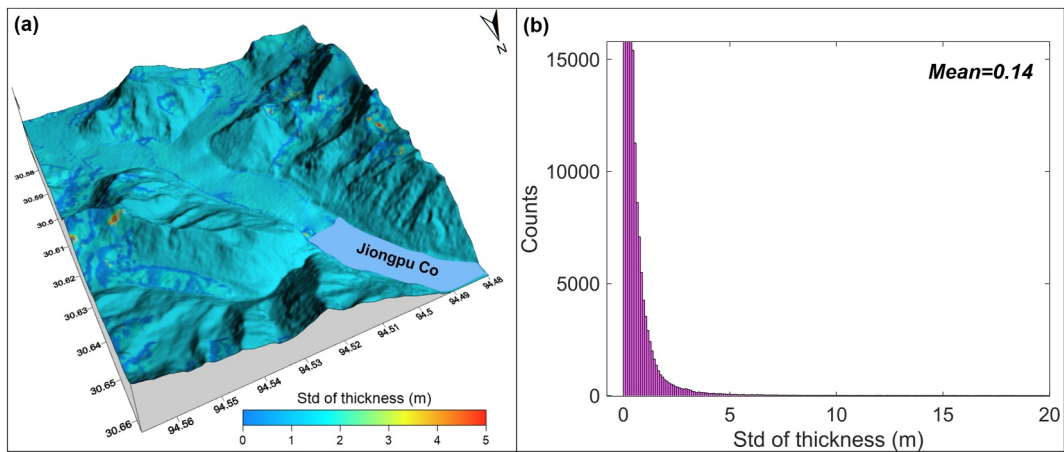


Figure 20. Uncertainties in thickness result. (a) Standard deviation of the glacier thickness. (b) Histogram of standard deviation of thickness.

Future efforts should prioritize integrated field campaigns to assess GLOF risk. Real-time lake-level monitoring systems should be deployed to track water-level fluctuations and downstream hydrological responses. GNSS networks can be established to monitor deformation in damming moraines. Additionally, high-resolution bathymetric surveys are essential for accurate hazard modeling. Remote sensing methods should be continuously applied to monitor lake expansion, adjacent slope stability, and glacier retreat dynamics to mitigate GLOF impacts.

6. Conclusions

GLOFs initiated by cascading processes represent a growing hazard in rapidly warming high-mountain regions. This study presents an integrated framework that combines remote sensing-derived glacier and slope dynamics with physically based flood modeling, enabling more precise assessments of multi-stage GLOF risks. Our approach not only improves the understanding of overtopping mechanisms caused by glacial and landslide movements but also offers transferable methodologies for assessing GLOF hazards in other glacial lake systems experiencing accelerating cryospheric change.

In our work, we conducted detailed monitoring and modeling of the potential GLOF hazard chain at Jiongpu Co in southeastern Tibet using multiple remote sensing methods and hydrographic measurements. First, a more than twofold increase in lake area was documented from 2000 to 2024. Second, we obtained 3-D glacier velocities and displacement time series to reveal the spatiotemporal evolution of glacier motion. The volume of the potential glacial avalanche was calculated by integrating SAR-derived ice thickness and terrain slope criteria, yielding $1.8 \pm 0.06 \times 10^8 \text{ m}^3$. Moreover, deformation rates and time series of surrounding slopes were monitored to assess slope destabilization. Seasonal deformation time series exhibited significant responses to temperature variations. Combining the deformed area with empirical area-volume relationships estimated a maximum landslide volume of $3.5 \pm 0.2 \times 10^8 \text{ m}^3$. Subsequently, we derived overtopping volumes from glacial avalanche and landslide movements into the lake using calculated initial source volumes. The results indicate that the overtopping volumes are $1.94 \pm 0.1 \times 10^7 \text{ m}^3$ and $9.89 \pm 0.6 \times 10^7 \text{ m}^3$, respectively. Finally, we simulated GLOF processes with the HEC-RAS model to evaluate downstream flood flow and depth. Our hydrodynamic modeling analysis indicated that landslide-induced GLOFs produce larger high-intensity inundation areas compared with glacier avalanche scenarios.

It is important to note that predictions of GLOF chains from mass movement into lakes are subject to considerable uncertainty. Our study presents methodologies for quantifying potential glacial avalanche and landslide volumes by bridging satellite-based remote sensing measurements with GLOF hazard simulations. Our research advances the understanding of initial mass movement dynamics in GLOF chains, characterizes overtopping wave generation from ice and rock inputs, and quantifies flood propagation processes in climate-warming high-mountain regions.

Conflict of Interest

The authors declare no conflicts of interest relevant to this study.

Data Availability Statement

Sentinel-1 data were provided by ASF (<https://search.asf.alaska.edu/#/>). The following parameters were used to search for Sentinel-1 ascending data set: File Type—“L1 SLC,” Beam Mode—“IW,” Direction—“Ascending,” Path #—70, and Frame #—1282. Similarly, the following parameters were used to search for Sentinel-1 descending data set: File Type—“L1 SLC,” Beam Mode—“IW,” Direction—“Descending,” Path #—4, and Frame #—491. Landsat-based optical images were acquired from USGS (<https://earthexplorer.usgs.gov/>) by entering geographic coordinates (30°39'16"N, 094°29'27"E) in the “Add Coordinates” menu. Lake inventory data were obtained from the National Special Environment and Function of Observation and Research Stations Shared Service Platform (China) (<https://doi.org/10.12072/casnw.064.2019.db>) (X. Wang et al., 2020). C-band SRTM DEMs were obtained from CGIAR-CSI (<https://opentopography.org/>), accessed via the “Global and Regional DEM” catalog: select “FIND DATA MAP” from the “DATA” menu and enter the minimum and maximum latitude and longitude as shown in Figure 1. ALOS PALSAR Radiometric Terrain Correction DEMs were retrieved from ASF (<https://search.asf.alaska.edu/#/>) by selecting “ALOS PALSAR” under Data sets, and “Hi-Res Terrain Corrected” under File Type. Historical daily weather temperatures were obtained from the meteorological website (<https://lishi.tianqi.com/bomi/index.html>) by choosing “Bomi, Tibet, China” from the City menu. Precipitation measurements were sourced from the Global Precipitation Measurement (GPM) satellite products (<https://gpm.nasa.gov/data/directory>) (Skofronick et al., 2017). The HEC-RAS software is publicly available from the official website of the U.S. Army Corps of Engineers (<https://www.hec.usace.army.mil/software/hec-ras/>) by navigating to the “Downloads” section.

Acknowledgments

This research is funded by the Scientific Research Foundation for Young Scholars of Xiangtan University (No. KZ0807569), and the NSFC (Grants 42022054, 42304026).

References

- Ali, E., Xu, W., & Ding, X. (2020). Improved optical image matching time series inversion approach for monitoring dune migration in North Sinai Sand Sea: Algorithm procedure, application, and validation. *ISPRS Journal of Photogrammetry and Remote Sensing*, 164, 106–124. <https://doi.org/10.1016/j.isprsjprs.2020.04.004>
- Allen, S., Frey, H., & Huggel, C. (2017). Assessment of glacier and permafrost hazards in mountain regions—technical guidance document. In *Standing group on glacier and permafrost hazards in mountains (GAPHAZ) of the International Association of Cryospheric Sciences (IACS) and the International Permafrost Association (IPA)* (p. 102962). Zurich.
- Allen, S. K., Cox, S. C., & Owens, I. F. (2011). Rock avalanches and other landslides in the central Southern Alps of New Zealand: A regional study considering possible climate change impacts. *Landslides*, 8(1), 33–48. <https://doi.org/10.1007/s10346-010-0222-z>
- Allen, S. K., Zhang, G., Wang, W., Yao, T., & Bolch, T. (2019). Potentially dangerous glacial lakes across the Tibetan Plateau revealed using a large-scale automated assessment approach. *Science Bulletin*, 64(7), 435–445. <https://doi.org/10.1016/j.scib.2019.03.011>
- Antoniazzi, G., & Lane, S. N. (2021). Sediment yield over glacial cycles: A conceptual model. *Progress in Physical Geography: Earth and Environment*, 45(6), 842–865. <https://doi.org/10.1177/0309133321997292>
- Azadnejad, S., Maghsoudi, Y., & Perissin, D. (2020). Evaluation of polarimetric capabilities of dual polarized Sentinel-1 and TerraSAR-X data to improve the PSInSAR algorithm using amplitude dispersion index optimization. *International Journal of Applied Earth Observation and Geoinformation*, 84, 101950. <https://doi.org/10.1016/j.jag.2019.101950>
- Bahr, D. B., Meier, M. F., & Peckham, S. D. (1997). The physical basis of glacier volume-area scaling. *Journal of Geophysical Research*, 102(B9), 20355–20362. <https://doi.org/10.1029/97jb01696>
- Benn, D. I., Warren, C. R., & Mottram, R. H. (2007). Calving processes and the dynamics of calving glaciers. *Earth-Science Reviews*, 82(3–4), 143–179. <https://doi.org/10.1016/j.earscirev.2007.02.002>
- Berardino, P., Fornaro, G., Lanari, R., & Sansosti, E. (2002). A new algorithm for surface deformation monitoring based on small baseline differential SAR interferograms. *IEEE Transactions on Geoscience and Remote Sensing*, 40(11), 2375–2383. <https://doi.org/10.1109/tgrs.2002.803792>
- Carrivick, J. L., & Tweed, F. S. (2013). Proglacial lakes: Character, behaviour and geological importance. *Quaternary Science Reviews*, 78, 34–52. <https://doi.org/10.1016/j.quascirev.2013.07.028>
- Chang, L., & Hanssen, R. F. (2015). A probabilistic approach for InSAR time-series postprocessing. *IEEE Transactions on Geoscience and Remote Sensing*, 54(1), 421–430. <https://doi.org/10.1109/tgrs.2015.2459037>
- Chen, F., Zhang, M., Guo, H., Allen, S., Kargel, J. S., Haritashya, U. K., & Watson, C. S. (2021). Annual 30 m dataset for glacial lakes in High Mountain Asia from 2008 to 2017. *Earth System Science Data*, 13(2), 741–766. <https://doi.org/10.5194/essd-13-741-2021>
- Chen, H., Cui, P., Chen, X., & Tang, J. (2017). Study on the surge wave induced by glacier avalanches and its effects on dam failure process. *International Journal of Erosion Control Engineering*, 10(1), 9–15. <https://doi.org/10.13101/ijece.10.9>
- Coe, J. A., Bessette-Kirton, E. K., & Geertsema, M. (2018). Increasing rock-avalanche size and mobility in Glacier Bay National Park and Preserve, Alaska detected from 1984 to 2016 Landsat imagery. *Landslides*, 15(3), 393–407. <https://doi.org/10.1007/s10346-017-0879-7>
- Cook, K. L., Andermann, C., Gimbert, F., Adhikari, B. R., & Hovius, N. (2018). Glacial lake outburst floods as drivers of fluvial erosion in the Himalaya. *Science*, 362(6410), 53–57. <https://doi.org/10.1126/science.aat4981>
- Dai, C., Higman, B., Lynett, P. J., Jacquemart, M., Howat, I. M., Liljedahl, A. K., et al. (2020). Detection and assessment of a large and potentially tsunamigenic periglacial landslide in Barry Arm, Alaska. *Geophysical Research Letters*, 47(22), e2020GL089800. <https://doi.org/10.1029/2020gl089800>

- Delaney, K. B., & Evans, S. G. (2015). The 2000 Yigong landslide (Tibetan Plateau), rockslide-dammed lake and outburst flood: Review, remote sensing analysis, and process modelling. *Geomorphology*, 246, 377–393. <https://doi.org/10.1016/j.geomorph.2015.06.020>
- Delbridge, B. G., Bürgmann, R., Fielding, E., Hensley, S., & Schulz, W. H. (2016). Three-dimensional surface deformation derived from airborne interferometric UAVSAR: Application to the Slumgullion Landslide. *Journal of Geophysical Research: Solid Earth*, 121(5), 3951–3977. <https://doi.org/10.1002/2015jb012559>
- Du, Z., Li, W., Zhou, D., Tian, L., Ling, F., Wang, H., et al. (2014). Analysis of Landsat-8 OLI imagery for land surface water mapping. *Remote Sensing Letters*, 5(7), 672–681. <https://doi.org/10.1080/2150704x.2014.960606>
- Emmer, A. (2017). Glacier retreat and glacial lake outburst floods (GLOFs). In *Oxford research encyclopedia of natural hazard science*.
- Farinotti, D., Brinkerhoff, D. J., Clarke, G. K., Fürst, J. J., Frey, H., Gantayat, P., et al. (2017). How accurate are estimates of glacier ice thickness? Results from ITMIX, the Ice Thickness Models Intercomparison experiment. *The Cryosphere*, 11(2), 949–970. <https://doi.org/10.5194/tc-11-949-2017>
- Farinotti, D., Brinkerhoff, D. J., Fürst, J. J., Gantayat, P., Gillet-Chaulet, F., Huss, M., et al. (2021). Results from the ice thickness models intercomparison experiment phase 2 (ITMIX2). *Frontiers in Earth Science*, 8, 571923. <https://doi.org/10.3389/feart.2020.571923>
- Ferretti, A., Prati, C., & Rocca, F. (2001). Permanent scatterers in SAR interferometry. *IEEE Transactions on Geoscience and Remote Sensing*, 39(1), 8–20. <https://doi.org/10.1109/36.898661>
- Frey, H., Machguth, H., Huss, M., Huggel, C., Bajracharya, S., Bolch, T., et al. (2014). Estimating the volume of glaciers in the Himalayan–Karakoram region using different methods. *The Cryosphere*, 8(6), 2313–2333. <https://doi.org/10.5194/tc-8-2313-2014>
- Froehlich, D. (1995). Peak outflow from breached embankment dam. *Journal of Water Resources Planning and Management*, 121(1), 90–97. [https://doi.org/10.1061/\(ASCE\)0733-9496\(1995\)121:1\(90\)](https://doi.org/10.1061/(ASCE)0733-9496(1995)121:1(90))
- Fujita, K., Sakai, A., Nuimura, T., Yamaguchi, S., & Sharma, R. R. (2009). Recent changes in Imja Glacial Lake and its damming moraine in the Nepal Himalaya revealed by in situ surveys and multi-temporal ASTER imagery. *Environmental Research Letters*, 4(4), 045205. <https://doi.org/10.1088/1748-9326/4/4/045205>
- Fujita, K., Sakai, A., Takenaka, S., Nuimura, T., Surazakov, A. B., Sawagaki, T., & Yamanokuchi, T. (2013). Potential flood volume of Himalayan glacial lakes. *Natural Hazards and Earth System Sciences*, 13(7), 1827–1839. <https://doi.org/10.5194/nhess-13-1827-2013>
- Gardelle, J., Arnaud, Y., & Berthier, E. (2011). Contrasted evolution of glacial lakes along the Hindu Kush Himalaya mountain range between 1990 and 2009. *Global and Planetary Change*, 75(1–2), 47–55. <https://doi.org/10.1016/j.gloplacha.2010.10.003>
- Gariano, S. L., & Guzzetti, F. (2016). Landslides in a changing climate. *Earth-Science Reviews*, 162, 227–252. <https://doi.org/10.1016/j.earscirev.2016.08.011>
- Glen, J. W. (1955). The creep of polycrystalline ice. *Proceedings of the Royal Society of London. Series A. Mathematical and Physical Sciences*, 228(1175), 519–538.
- Guo, L., Li, J., Li, Z. W., Wu, L. X., Li, X., Hu, J., et al. (2020). The surge of the Hispar Glacier, Central Karakoram: SAR 3-D flow velocity time series and thickness changes. *Journal of Geophysical Research: Solid Earth*, 125(7), e2019JB018945. <https://doi.org/10.1029/2019JB018945>
- Hock, R., Rasul, G., Adler, C., Cáceres, B., Gruber, S., Hirabayashi, Y., et al. (2019). High mountain areas. In H.-O. Pörtner, D. C. Roberts, V. Masson-Delmotte, P. Zhai, M. Tignor, E. Poloczanska, et al. (Eds.), *IPCC special report on the ocean and cryosphere in a changing climate* (pp. 131–202).
- Hooper, A. (2008). A multi-temporal InSAR method incorporating both persistent scatterer and small baseline approaches. *Geophysical Research Letters*, 35(16). <https://doi.org/10.1029/2008gl034654>
- Hooper, A., Zebker, H., Segall, P., & Kampes, B. (2004). A new method for measuring deformation on volcanoes and other natural terrains using InSAR persistent scatterers. *Geophysical Research Letters*, 31(23). <https://doi.org/10.1029/2004gl021737>
- Hooper, A., & Zebker, H. A. (2007). Phase unwrapping in three dimensions with application to InSAR time series. *JOSA A*, 24(9), 2737–2747. <https://doi.org/10.1364/josaa.24.002737>
- Hu, X., Bürgmann, R., Lu, Z., Handwerger, A. L., Wang, T., & Miao, R. (2019). Mobility, thickness, and hydraulic diffusivity of the slow-moving Monroe landslide in California revealed by L-band satellite radar interferometry. *Journal of Geophysical Research: Solid Earth*, 124(7), 7504–7518. <https://doi.org/10.1029/2019jb017560>
- Hu, X., Lu, Z., Pierson, T. C., Kramer, R., & George, D. L. (2018). Combining InSAR and GPS to determine transient movement and thickness of a seasonally active low-gradient translational landslide. *Geophysical Research Letters*, 45(3), 1453–1462. <https://doi.org/10.1002/2017gl076623>
- Hugonet, R., McNabb, R., Berthier, E., Menounos, B., Nuth, C., Girod, L., et al. (2021). Accelerated global glacier mass loss in the early twenty-first century. *Nature*, 592(7856), 726–731. <https://doi.org/10.1038/s41586-021-03436-z>
- Immerzeel, W. W., Van Beek, L. P., & Bierkens, M. F. (2010). Climate change will affect the Asian water towers. *Science*, 328(5984), 1382–1385. <https://doi.org/10.1126/science.1183188>
- Iverson, R. M. (2000). Landslide triggering by rain infiltration. *Water Resources Research*, 36(7), 1897–1910. <https://doi.org/10.1029/2000wr900090>
- Jiskoot, H. (2011). Dynamics of glaciers. *Physical Research*, 92(B9), 9–083.
- Kääb, A., Leinss, S., Gilbert, A., Bühler, Y., Gascoin, S., Evans, S. G., et al. (2018). Massive collapse of two glaciers in western Tibet in 2016 after surge-like instability. *Nature Geoscience*, 11(2), 114–120. <https://doi.org/10.1038/s41561-017-0039-7>
- Kang, Y., Lu, Z., Zhao, C., & Qu, W. (2023). Inferring slip-surface geometry and volume of creeping landslides based on InSAR: A case study in Jinsha River basin. *Remote Sensing of Environment*, 294, 113620. <https://doi.org/10.1016/j.rse.2023.113620>
- Kim, J., Coe, J. A., Lu, Z., Avdievitch, N. N., & Hults, C. P. (2022). Spaceborne InSAR mapping of landslides and subsidence in rapidly deglaciating terrain, Glacier Bay National Park and Preserve and vicinity, Alaska and British Columbia. *Remote Sensing of Environment*, 281, 113231. <https://doi.org/10.1016/j.rse.2022.113231>
- Kohanpur, A. H., Saksena, S., Dey, S., Johnson, J. M., Riasi, M. S., Yeghiazarian, L., & Tartakovsky, A. M. (2023). Urban flood modeling: Uncertainty quantification and physics-informed Gaussian processes regression forecasting. *Water Resources Research*, 59(3), e2022WR033939. <https://doi.org/10.1029/2022wr033939>
- Korup, O. (2006). Effects of large deep-seated landslides on hillslope morphology, western Southern Alps, New Zealand. *Journal of Geophysical Research*, 111(F1). <https://doi.org/10.1029/2004jf000242>
- Li, D., Lu, X., Walling, D. E., Zhang, T., Steiner, J. F., Wasson, R. J., et al. (2022). High Mountain Asia hydropower systems threatened by climate-driven landscape instability. *Nature Geoscience*, 15(7), 520–530. <https://doi.org/10.1038/s41561-022-00953-y>
- Li, J., Li, Z. W., Wu, L. X., Xu, B., Hu, J., Zhou, Y. S., & Miao, Z. L. (2018). Deriving a time series of 3D glacier motion to investigate interactions of a large mountain glacial system with its glacial lake: Use of Synthetic Aperture Radar Pixel Offset-Small Baseline Subset technique. *Journal of Hydrology*, 559, 596–608. <https://doi.org/10.1016/j.jhydrol.2018.02.067>

- Li, W., Du, Z., Ling, F., Zhou, D., Wang, H., Gui, Y., et al. (2013). A comparison of land surface water mapping using the normalized difference water index from TM, ETM+ and ALI. *Remote Sensing*, 5(11), 5530–5549. <https://doi.org/10.3390/rs5115530>
- Li, Y., Cui, Y., Hu, X., Lu, Z., Guo, J., Wang, Y., et al. (2024). Glacier retreat in Eastern Himalaya drives catastrophic glacier hazard chain. *Geophysical Research Letters*, 51(8), e2024GL108202. <https://doi.org/10.1029/2024GL108202>
- Liu, W., Carling, P. A., Hu, K., Wang, H., Zhou, Z., Zhou, L., et al. (2019). Outburst floods in China: A review. *Earth-Science Reviews*, 197, 102895. <https://doi.org/10.1016/j.earscirev.2019.102895>
- Lu, X., Zhou, G. G., Cui, K. F., Tang, H., & Xie, Y. (2022). Overtopping volume of impulse waves in glacier lakes: Experimental and numerical investigation using rigid dams. *Engineering Geology*, 306, 106763. <https://doi.org/10.1016/j.enggeo.2022.106763>
- Lu, Z., & Kim, J. (2021). A framework for studying hydrology-driven landslide hazards in northwestern US using satellite InSAR, precipitation and soil moisture observations: Early results and future directions. *GeoHazards*, 2(2), 17–40. <https://doi.org/10.3390/geohazards2020002>
- Luo, L. H., Ke, C. Q., Fan, Y. B., & Wang, Z. F. (2023). Accelerated glacier mass loss in the southeastern Tibetan Plateau since the 1970s. *Advances in Climate Change Research*, 14(3), 372–386. <https://doi.org/10.1016/j.accre.2023.04.007>
- Matsuoka, N., & Murton, J. (2008). Frost weathering: Recent advances and future directions. *Permafrost and Periglacial Processes*, 19(2), 195–210. <https://doi.org/10.1002/ppb.620>
- Millan, R., Mouginot, J., Rabatel, A., & Morlighem, M. (2022). Ice velocity and thickness of the world's glaciers. *Nature Geoscience*, 15(2), 124–129. <https://doi.org/10.1038/s41561-021-00885-z>
- Morlighem, M., Rignot, E., Seroussi, H., Larour, E., Ben Dhia, H., & Aubry, D. (2011). A mass conservation approach for mapping glacier ice thickness. *Geophysical Research Letters*, 38(19). <https://doi.org/10.1029/2011gl048659>
- Nie, Y., Liu, Q., & Liu, S. (2013). Glacial lake expansion in the Central Himalayas by Landsat images, 1990–2010. *PLoS One*, 8(12), e83973. <https://doi.org/10.1371/journal.pone.0083973>
- Nie, Y., Liu, Q., Wang, J., Zhang, Y., Sheng, Y., & Liu, S. (2018). An inventory of historical glacial lake outburst floods in the Himalayas based on remote sensing observations and geomorphological analysis. *Geomorphology*, 308, 91–106. <https://doi.org/10.1016/j.geomorph.2018.02.002>
- Pánek, T., & Klimeš, J. (2016). Temporal behavior of deep-seated gravitational slope deformations: A review. *Earth-Science Reviews*, 156, 14–38. <https://doi.org/10.1016/j.earscirev.2016.02.007>
- Peng, M., Wang, X., Zhang, G., Veh, G., Sattar, A., Chen, W., & Allen, S. (2023). Cascading hazards from two recent glacial lake outburst floods in the Nyainqntanglha range, Tibetan Plateau. *Journal of Hydrology*, 626, 130155. <https://doi.org/10.1016/j.jhydrol.2023.130155>
- Qin, X., Huang, Y., Wang, C., Jiang, K., Xie, L., Liu, R., et al. (2024). A temporary soil dump settlement and landslide risk analysis using the improved small baseline subset-InSAR and continuous medium model. *International Journal of Applied Earth Observation and Geoinformation*, 128, 103760. <https://doi.org/10.1016/j.jag.2024.103760>
- Qu, F., Lu, Z., Kim, J., & Turco, M. J. (2023). Mapping and characterizing land deformation during 2007–2011 over the Gulf Coast by L-band InSAR. *Remote Sensing of Environment*, 284, 113342. <https://doi.org/10.1016/j.rse.2022.113342>
- Rounce, D. R., McKinney, D. C., Lala, J. M., Byers, A. C., & Watson, C. S. (2016). A new remote hazard and risk assessment framework for glacial lakes in the Nepal Himalaya. *Hydrology and Earth System Sciences*, 20(9), 3455–3475. <https://doi.org/10.5194/hess-20-3455-2016>
- Samsonov, S., Tiampo, K., & Cassotto, R. (2021). SAR-derived flow velocity and its link to glacier surface elevation change and mass balance. *Remote Sensing of Environment*, 258, 112343. <https://doi.org/10.1016/j.rse.2021.112343>
- Sattar, A., Allen, S., Mergili, M., Haeberli, W., Frey, H., Kulkarni, A. V., et al. (2023). Modeling potential glacial lake outburst flood process chains and effects from artificial lake-level lowering at Gepang Gath Lake, Indian Himalaya. *Journal of Geophysical Research: Earth Surface*, 128(3), e2022JF006826. <https://doi.org/10.1029/2022jf006826>
- Sattar, A., Haritashya, U. K., Kargel, J. S., & Karki, A. (2022). Transition of a small Himalayan glacier lake outburst flood to a giant transborder flood and debris flow. *Scientific Reports*, 12(1), 12421. <https://doi.org/10.1038/s41598-022-16337-6>
- Savi, S., Comiti, F., & Strecker, M. R. (2021). Pronounced increase in slope instability linked to global warming: A case study from the eastern European Alps. *Earth Surface Processes and Landforms*, 46(7), 1328–1347. <https://doi.org/10.1002/esp.5100>
- Shugar, D. H., Jacquemart, M., Shean, D., Bhushan, S., Upadhyay, K., Sattar, A., et al. (2021). A massive rock and ice avalanche caused the 2021 disaster at Chamoli, Indian Himalaya. *Science*, 373(6552), 300–306. <https://doi.org/10.1126/science.abh4455>
- Skofronick-Jackson, G., Petersen, W. A., Berg, W., Kidd, C., Stocker, E. F., Kirschbaum, D. B., et al. (2017). The Global Precipitation Measurement (GPM) mission for science and society. *Bulletin of the American Meteorological Society*, 98(8), 1679–1695. <https://doi.org/10.1175/bams-d-15-0306.1>
- Stoffel, M., & Huggel, C. (2012). Effects of climate change on mass movements in mountain environments. *Progress in Physical Geography*, 36(3), 421–439. <https://doi.org/10.1177/030913312441010>
- Stoffel, M., Trappmann, D. G., Coullie, M. I., Ballesteros Cánovas, J. A., & Corona, C. (2024). Rockfall from an increasingly unstable mountain slope driven by climate warming. *Nature Geoscience*, 17(3), 249–254. <https://doi.org/10.1038/s41561-024-01390-9>
- Sun, M., Liu, S., & Yao, X. (2014). The cause and potential hazard of glacial lake outburst flood occurred on July 5, 2013 in Jiali County, Tibet. *Journal of Glaciology and Geocryology*, 36(1), 158–165.
- Tseng, C. M., Lin, C. W., Stark, C. P., Liu, J. K., Fei, L. Y., & Hsieh, Y. C. (2013). Application of a multi-temporal, LiDAR-derived, digital terrain model in landslide-volume estimation. *Earth Surface Processes and Landforms*, 38(13), 1587–1601. <https://doi.org/10.1002/esp.3454>
- Van Asch, T. W., Buma, J., & Van Beek, L. P. H. (1999). A view on some hydrological triggering systems in landslides. *Geomorphology*, 30(1–2), 25–32. [https://doi.org/10.1016/S0169-555X\(99\)00042-2](https://doi.org/10.1016/S0169-555X(99)00042-2)
- Wang, W., Gao, Y., Anacona, P. I., Lei, Y., Xiang, Y., Zhang, G., et al. (2018). Integrated hazard assessment of Cirenmaco glacial lake in Zhangzangbo valley, Central Himalayas. *Geomorphology*, 306, 292–305. <https://doi.org/10.1016/j.geomorph.2015.08.013>
- Wang, X., Guo, X., Yang, C., Liu, Q., Wei, J., Zhang, Y., et al. (2020). Glacial lake inventory of high-mountain Asia in 1990 and 2018 derived from Landsat images [Dataset]. *Earth System Science Data*, 12(3), 2169–2182. <https://doi.org/10.12072/casnw.064.2019.db>
- Wang, X., & Liu, S. Y. (2016). Evaluation method and application of moraine-dammed lake outburst disaster in Himalaya Range.
- Yan, S., Liu, G., Wang, Y., & Ruan, Z. (2015). Accurate determination of glacier surface velocity fields with a DEM-assisted pixel-tracking technique from SAR imagery. *Remote Sensing*, 7(8), 10898–10916. <https://doi.org/10.3390/rs70810898>
- Yang, L., Lu, Z., Ouyang, C., Zhao, C., Hu, X., & Zhang, Q. (2023). Glacial lake outburst flood monitoring and modeling through integrating multiple remote sensing methods and HEC-RAS. *Remote Sensing*, 15(22), 5327. <https://doi.org/10.3390/rs15225327>
- Yang, L., Lu, Z., Zhao, C., Kim, J., Yang, C., Wang, B., et al. (2022). Analyzing the triggering factors of glacial lake outburst floods with SAR and optical images: A case study in Jinweng Co, Tibet, China. *Landslides*, 19(4), 855–864. <https://doi.org/10.1007/s10346-021-01831-1>
- Yang, L., Zhao, C., Lu, Z., Yang, C., & Zhang, Q. (2020). Three-dimensional time series movement of the cuolangma glaciers, southern Tibet with Sentinel-1 imagery. *Remote Sensing*, 12(20), 3466. <https://doi.org/10.3390/rs12203466>
- Yang, W., Yao, T., Guo, X., Zhu, M., Li, S., & Kattel, D. B. (2013). Mass balance of a maritime glacier on the southeast Tibetan Plateau and its climatic sensitivity. *Journal of Geophysical Research: Atmospheres*, 118(17), 9579–9594. <https://doi.org/10.1002/jgrd.50760>

- Zekollari, H., Huss, M., Farinotti, D., & Lhermitte, S. (2022). Ice-dynamical glacier evolution modeling—A review. *Reviews of Geophysics*, 60(2), e2021RG000754. <https://doi.org/10.1029/2021rg000754>
- Zhang, G., Bolch, T., Yao, T., Rounce, D. R., Chen, W., Veh, G., et al. (2023). Underestimated mass loss from lake-terminating glaciers in the greater Himalaya. *Nature Geoscience*, 16(4), 333–338. <https://doi.org/10.1038/s41561-023-01150-1>
- Zhang, G., Yao, T., Xie, H., Wang, W., & Yang, W. (2015). An inventory of glacial lakes in the Third Pole region and their changes in response to global warming. *Global and Planetary Change*, 131, 148–157. <https://doi.org/10.1016/j.gloplacha.2015.05.013>
- Zheng, G., Allen, S. K., Bao, A., Ballesteros-Cánovas, J. A., Huss, M., Zhang, G., et al. (2021). Increasing risk of glacial lake outburst floods from future Third Pole deglaciation. *Nature Climate Change*, 11(5), 411–417. <https://doi.org/10.1038/s41558-021-01028-3>